Chapter 2
Tool Influence Functions

Abstract This chapter investigates the tool influence functions (TIFs) and analyzes relevant assessment criteria from the aspect of removal capability. Then, with respect to different optical surfacing systems, TIF theoretical models were constructed and validated by experiments. A series of key parameters were optimized to confirm the preferable TIF for deterministic finishing processes.

2.1 Front Matter for Tool Influence Functions

As mentioned in Chap. 1, the tool influence function (TIF) serves as an important and indispensable variable in the optical surfacing system. It represents the material removal produced by a polishing tool in a unit of time. In the practical polishing process, the TIF would be taken into the calculation of dwell time. Its peak removal rate (PRR) and shape would generate a huge influence on the magnitude and distribution of the dwell-time map.

Based on the Preston function presented in Chap. 1, the theoretical model of TIFs can be built through the corresponding motion model and pressure distribution model. According to the Fourier transform theory, we can conclude two important equations:

$$\widetilde{\mathrm{TIF}} = \int_{-\infty}^{\infty} \mathrm{TIF}(x, y)\ \mathrm{d}x\mathrm{d}y \tag{2.1}$$

$$\mathrm{TIF} = \int_{-\infty}^{\infty} \widetilde{\mathrm{TIF}}(\varepsilon, \eta)\ \mathrm{d}\varepsilon\mathrm{d}\eta \tag{2.2}$$

Equation (2.1) indicates that the direct current (DC) response of polishing systems is constructed by the integration of TIF in the space domain. The integration value is always non-negative because of the non-negativity of TIFs. We can obtain uniform material on the surface if uniform polishing is conducted on the surface. Equation (2.2) illustrates that a TIF with zero central removal can remove a

H. Cheng, *Independent Variables for Optical Surfacing Systems: Synthesis, Characterization and Application*, DOI 10.1007/978-3-642-45355-7_2,
© Springer-Verlag Berlin Heidelberg 2014

certain period of surface errors but leave more mid–high spatial frequency errors. If the TIF has central peak removal, the surface error can be convergent one-by-one with increasing polishing times.

Thus, from the above analysis, the basic characteristics of TIFs can be concluded as:

- A TIF should be a rotational-symmetric and smooth function.
- A TIF has central peak removal and decreases as the radius increases.
- A TIF has no material removal when the distance exceeds the maximum radius.
- The slope of a TIF at the center and edge regions should be zero.

Since the 1970s, people have taken more than 40 years to find an ideal polishing tool with perfect TIFs. New tools with different work principles emerge every few years. Their purpose is only to improve the performance of material removal on removal rate, roughness, free-edge effect, non-subsurface damage, and stability. Removal rate directly affects the fabrication efficiency, which is referred to as the primary purpose to some extent. The roughness performance is also significant; it influences the distribution of high-spatial frequency errors, which has strict demands in x-ray and laser gyroscope systems. The ideal polishing tool should also have no subsurface damage to ensure that no damage exists on the subsurface of optical segments, as this damage would diminish the long-term stability of optical systems and the coating quality, image performance, and laser-induced damage threshold of optical elements. Contact-type polishing tools remove material by relying on contact pressure, which results in an edge effect when the tool dwells in the edge region of the segment. Stability also serves as an indispensable target, as the convergence rate of surface form would largely decrease if the stability of the TIF is low. The ideal TIF should always remain invariant during the entire fabrication.

2.2 The Assessment Criteria of a TIF

2.2.1 Peak and Volume Removal Rate

A TIF represents the distribution of the material removal rate across the size of the polishing tool in a unit of time. It is often characterized by two parameters; the first is the PRR, which is the maximum removal rate, as presented in Eq. (2.3).

$$\mathrm{PRR} = \max(\mathrm{TIF}) \tag{2.3}$$

The other is the volume removal rate (VRR), which is the sum of all values in the data array multiplied by the cell scale squared, as described in Eq. (2.4). If the shape remains invariant, the VRR would be linear proportional to the increasing PRR.

$$\mathrm{VRR} = \sum_{i=1}^{m}\sum_{j=1}^{n} \mathrm{TIF}(i,j) \cdot \Delta x \cdot \Delta y \tag{2.4}$$

2.2.2 Central-Peak Factor for Removal Capability

Generally, a TIF possessing central peak material removal has a more powerful capability to figure small errors of a surface form. To describe it quantitatively, a central-peak factor is defined as:

$$F_{\mathrm{cpf}} = \frac{\int_{-r/4}^{r/4} \mathrm{TIF}(r)\mathrm{d}r}{\int_{-r}^{r} \mathrm{TIF}(r)\mathrm{d}r} \tag{2.5}$$

where r represents the half-size of the TIF. A large central-peak factor means the TIF is highly centralized and has more power to figure the surface form.

2.2.3 Cutoff Frequency for Removal Capability

The removal capability of a TIF for localized residual errors has great significance for high fabrication accuracy of optical surfaces. From this view, the best TIF should be a pulsing function that which could correct any localized residual errors. However, we could not obtain a pulsing TIF in any case. If a TIF performs closer to a pulsing function, it has much higher removal capability for localized residual errors. For a certain size TIF, the shape has a large influence on the removal capability. From the frequency domain, the normalized amplitude frequency spectrum of a TIF can be expressed as:

$$\mathrm{TIF}_F(w) = \mathrm{FFT}(\mathrm{TIF}_n(r)) \tag{2.6}$$

where FFT represents Fast Fourier Transform, and $\mathrm{TIF}_n(r)$ represents the normalized TIF. An example of a normalized amplitude frequency spectrum curve is shown in Fig. 2.1.

Figure 2.1a displays a typical TIF. Figure 2.1b is the corresponding normalized amplitude frequency spectrum curve, which quickly drops down to near-zero. For a specific spatial frequency, a higher normalized amplitude represents a higher removal capability for localized small errors.

The cutoff frequency represents the specific spatial frequency where the normalized amplitude spectrum curve reduces to 0.05 (point A shown in Fig. 2.1b); we consider that the TIF could not generate a valid correction for the localized error whose spatial frequency exceeds the cutoff frequency. For a TIF with a certain size, the cutoff frequency could evaluate the removal capability for localized errors. A higher cutoff frequency means higher removal capability for localized small errors.

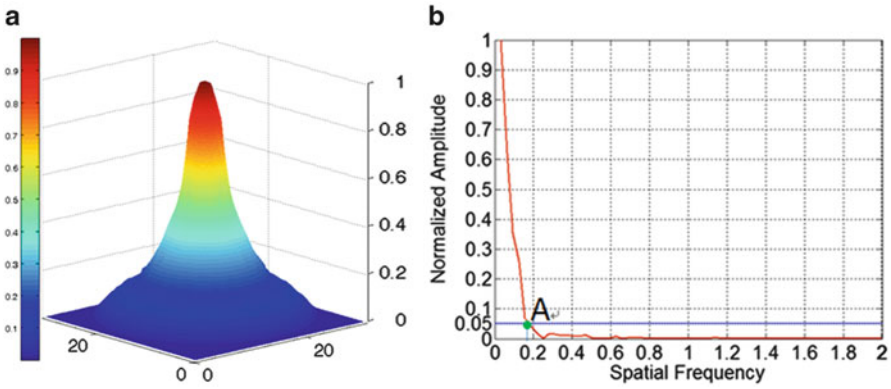

Fig. 2.1 An example of normalized amplitude frequency spectrum curve. (**a**) The typical TIF; (**b**) its corresponding normalized amplitude frequency spectrum curve. *TIF* tool influence function

2.3 TIF Model Constructions and Optimizations

2.3.1 Computer-Controlled Polishing with Small Tools

2.3.1.1 System Descriptions and TIF Model Construction

Computer-controlled polishing with small tools is regarded as the premier computer-controlled optical surfacing (CCOS) technology which has been investigated in detail in the US since 1970 [1, 2] and then been developed widely all over the world. This technique breaks the problems of traditional handmade and single-axis machines in both fabrication efficiency and surface precision, and especially devotes to the fabrication of large aspheric mirrors. China has been pursuing this advanced fabricating technique since 1990. After 20 years of development, several generation systems have been developed.

Figure 2.2 shows an overall structure photograph and movement schematic view of the computer numerical control (CNC) machining system developed in the 1990s. The system is arranged as a gantry structure—two pillars, a crossbeam and a base form the main frame of the machine. Taking machining and measuring stability and performance into consideration, Chinese Tai Shan Qing (TSQ) marble blocks, as the selected material, are shaped into parts of the machine frame. Based on the idea of deterministic manufacture, the tool's self-rotation axis should always trace the normal line of the aspheric surface across the whole working area in order to achieve the required accuracy with high material removal efficiency. Therefore, the system is designed to be controlled on six axes: (1) the tool's self-rotation around its axis at a rotational speed of W_2; (2) the tool's swing around the X-axis; (3) the tool's motion in the Y-axis; (4) the tool's motion along its axis; (5) the turntable's rotation around its axis at a rotational speed of W_1; and (6) the turntable's motion in X direction. Furthermore, a profiler equipped with dual touch-trigger probe (Heidenhain Co., Ltd, Germany) is installed in the system for on-machine profile measurement during the grinding process, which is also an innovating issue of the system.

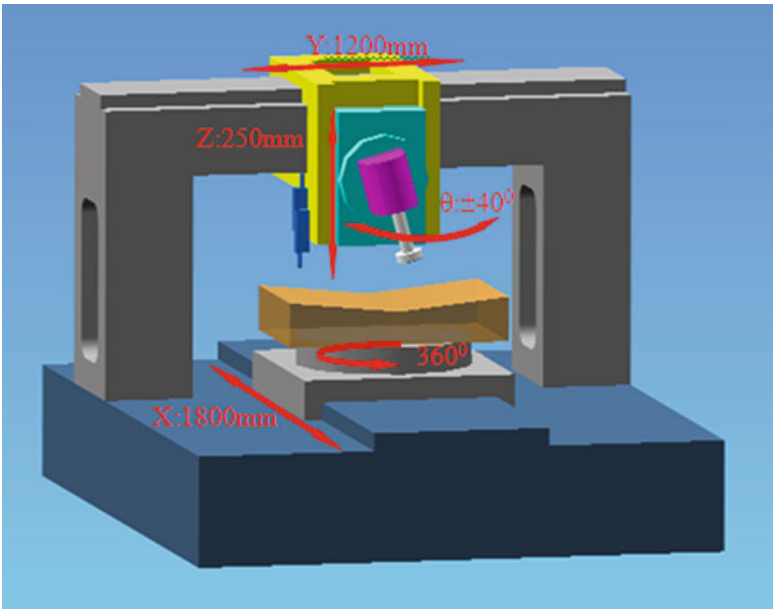

Fig. 2.2 Movement schematic view of the computer numerical control (CNC) machining system (Reproduced from Cheng et al. [7])

Table 2.1 Functions and specification of the machining system

Number of working axials	Stroke in X direction	Stroke in Y direction	Stretch of tool in its axis	Online testing	Range of swing angle	Surfacing off-axial optics
6	1.8 m	1.2 m	0.25 m	Contact	±40°	Yes

The system combined the faculties of grinding, fine grinding, polishing, and on-machine profile measuring. The sub-aperture tool is driven with two motors. One is for the tool's swing around the X-axis, and the other is for the self-rotation of the tool around its axis. Meanwhile, a workpiece held on the turntable is rotated at the speed of W_1 under the polar coordinate (for the workpiece shaped with rotary symmetry), or moved straight in X direction under the Cartesian coordinate (for the workpiece shaped with non-rotary symmetry, i.e. rectangular shape). In order for the tool axis to always be the normal line of the aspheric surface, the concurrent control for the tool swing angle θ_i and the swing center position in Y direction is made available. The contact pressure between the tool and the workpiece is applied using an air cylinder mounted on the tool axis. Thus, a good fit between the tool and the workpiece is maintained as the tool moves along the aspheric surface. During machining operation, the loose abrasive is injected into the working area on the workpiece surface. The functions and specifications of the developed machining system are shown in Table 2.1. The profiler equipped with two touch-trigger

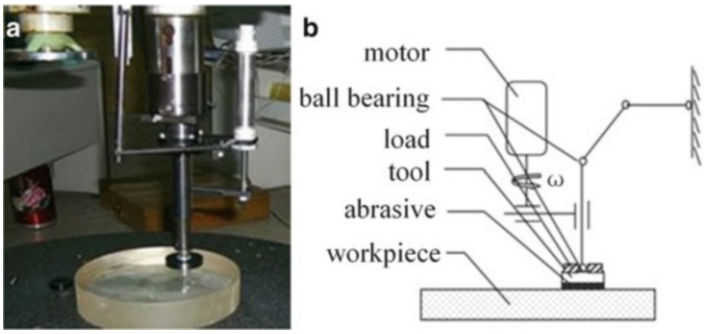

Fig. 2.3 Motion pictorial view. (**a**) The tool planar motion model; (**b**) its motion schematic view of the tool

Fig. 2.4 Sketch map of the tool's motion

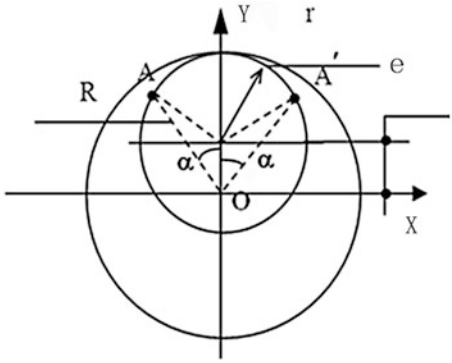

Heidenhain digital length probe assemblies are mounted on a translation stage, using a granite straight edge with high-precision linearity as the reference to reduce the linearity error of the ball slide.

The optimum TIF configuration is determined in order to produce a profile with a central peak and a fairly rapid decrease to zero. A method for generating the desired tool removal profiles was determined to be the epicyclic motion—dual rotations by Jones in 1977 [3]. The tool would rotate around its center at a rapid rate, while the entire mechanism would revolve around a secondary center at a slower rate. Here, a novel tool is designed to move in planar model enlightened from the traditional hand polishing. Figure 2.3a, b present a photograph and motion schematic view of the tool; its motion principle is different to the one in the Jones paper [3]. At the working start position, the tool would rotate around its center at a proper rate from position $+\alpha$ to $-\alpha$ in a clockwise direction driven by a servo motor, to achieve a good tool move orbit, there is often an off-centering distance between the axis of motor and tool, while a draw rod would draw back the tool rotate from position $-\alpha$ to $+\alpha$ in an anticlockwise direction; thus, the to-and-fro motion would be continued by virtue of the reciprocator.

In Fig. 2.4, r is the radius of the tool, e is the off-centering distance, during one machining cycle, the covered grinding or polishing area should be a circle with a radius of $r + e$ and centered as point O, for a random point A located in the

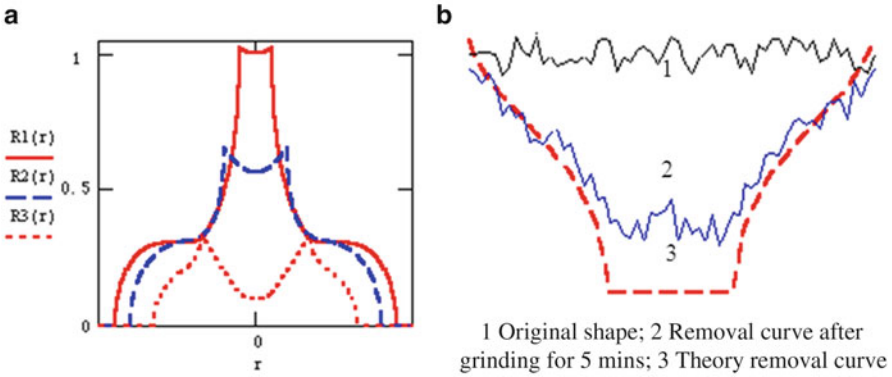

Fig. 2.5 (**a**) Simulation on removal rate with different e/r; (**b**) experimental result (Reproduced from Cheng et al. [7])

machining area from point O is distance R, the angle with Y direction is α. Therefore, the relative acting angle should be:

$$2\alpha = \begin{cases} 2\arccos\left(\dfrac{R^2 + e^2 - r^2}{2\mathrm{Re}}\right) & r - e < R \le r + e \\ 2\pi & 0 \le R \le r - e \end{cases} \tag{2.7}$$

According to the Preston hypothesis, the material removed under the grinding or polishing tool is given by

$$R(r) = KP\int_0^t V\mathrm{d}t \tag{2.8}$$

where K is the constant that depends on the tool and the workpiece materials and the grinding or polishing compounds, etc., P is the pressure at point A, V is the relative velocity between the tool and point on the workpiece, which is a constant equal to $w \times e$ in one machining cycle, from Eqs. (2.7) and (2.8).

$$\begin{aligned} R(r) &= KP\int_0^t (we)\frac{\mathrm{d}\alpha}{w} \\ &= \begin{cases} 2eKP\arccos\left(\dfrac{R^2 + e^2 - r^2}{2\mathrm{Re}}\right) & r - e < R \le r + e \\ 2\pi eKP & 0 \le R \le r - e \end{cases} \end{aligned} \tag{2.9}$$

To find out a set of optimum technical parameters, we designed three sets of curves (see Fig. 2.5a). $R1(r)$, $R2(r)$ and $R3(r)$ are achieved when e/r equals 0.72,

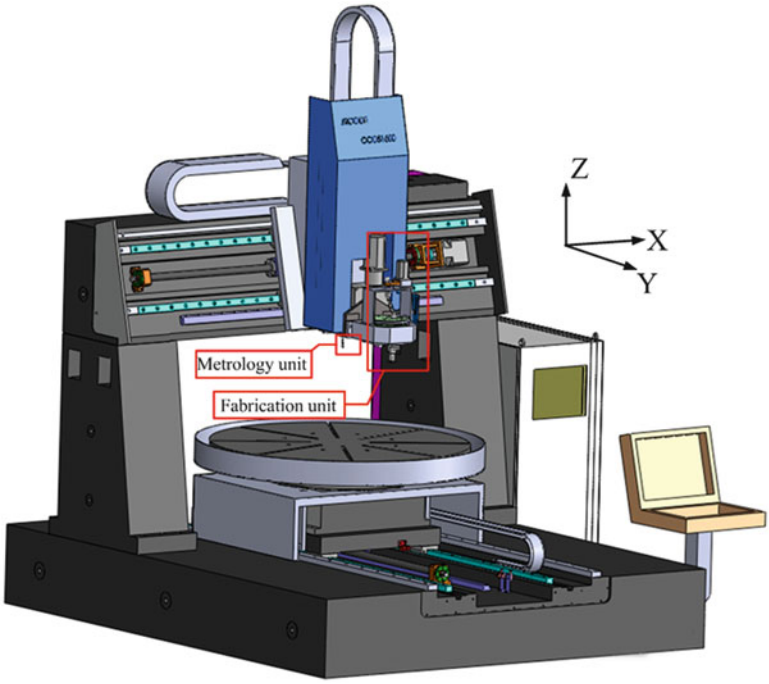

Fig. 2.6 Schematic illustration of JR-1800

0.85, and 1.00, respectively. It is easy to observe that the TIF curve $R1(r)$ with a higher central peak would result in successful machining. Choosing $e/r = 0.72$ as an optimum parameter, at a relative rotational speed $w = 20$ rpm (revolutions per minute), a grinding experiment is performed on a K9 glass for 5 min. The results shown in Fig. 2.5b also verify the selected optimum parameter has a proper removal feature.

Another typical system was built in 2012 (see Fig. 2.6), namely JR-1800. This system is a multifunctional and compound machine system with seven CNC axes. The system adopts a bridge structure on a base marble of 3, 200 mm $\times$ 4, 000 mm $\times$ 620 mm (weight: ~20 t), which supplies a highly stable fabrication and metrology environment. JR-1800 comprises five parts: a cross *XY*-axis (travel distance: 1, 840 mm $\times$ 2, 096 mm), a separate *Z*-axis (travel distance: 603 mm), a rotating turntable (diameter: 1,800 mm), a changeable profile metrology unit, and a fabrication unit. The location uncertaintities of *XYZ*-axis are controlled within 5 μm in their travel distance, and linearity is less than 2 μm in any 1,000 mm range.

The machine is capable of producing ultra-precise surfaces for a various of optical materials (e.g. silicon carbide (SiC), fused silica, Zerodur, etc.) and surface forms (plane, sphere, axisymmetric or off-axis aspherics). The maximal fabrication and metrology range reaches up to 1,800 mm. Compared with single-purpose machines, JR-1800 integrates fixed abrasive micro-lapping, loose abrasive polishing,

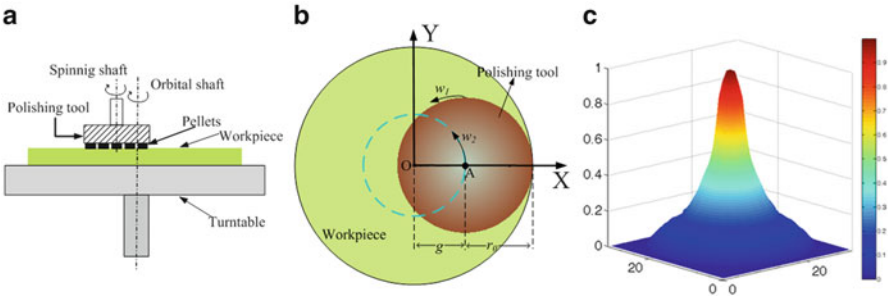

Fig. 2.7 Planetary motion model in deterministic lapping and polishing

and online metrology. It features advantages of (1) shorter fabrication or metrology duration; (2) diminishing the risk when carrying workpieces from one place to another; and (3) largely saving cost and floor space.

It is widely accepted that Gaussian-shape TIF is preferable in deterministic lapping/polishing. To achieve this characteristic, the fabrication unit employs a planetary motion model, as shown in Fig. 2.7a, b. The polishing pad (with semi-diameter r_0) executes self-rotation with respect to its spindle. The spinning velocity w_1 reaches up to 1,000 rpm. Simultaneously, the pad makes an orbital motion (orbital velocity w_2) with changeable orbital radius g. A typical Gaussian-shape TIF of JR-1800 is shown in Fig. 2.7c. With the exception of the spinning and orbital axes, the fabrication unit also employs a tilt axis to ensure that the spindle remains normal to curved surfaces.

This eccentric transmission of spinning is a tricky problem because high rigidity and torque are required for lapping/polishing of hard material. The conventional soft axis system is incompetent to transmit large torque, and lacks stability. We presented a retractable universal joint (represented as 4 in Fig. 2.8a and shown in detail in Fig. 2.8b). It comprises two portions: the upper joint and the lower joint. The upper joint can stretch out of the lower joint when the orbital radius increases. The upper motor (represented as 1 in Fig. 2.8a) drives the actuating shaft (represented as 3 in Fig. 2.8a), which is bounded together with the upper joint. The lower joint then drives the rotating spindle. The tail end of the spindle is a gas cylinder (represented as 5 in Fig. 2.8a). The press implemented on the polishing tool can be exactly controlled by the air pressure.

Fixed abrasive fabrication technology has been developed for tens of years, and was recently used in the polishing of optical component. Compared with loose abrasive, fixed abrasive polishing brings in many improvements in removal rate and draws wide public attention. The influence of the polishing parameters to material removal rate and surface roughness of fixed abrasive polishing has been studied extensively. Based on CCOS technology, people take the place of pitch pads with fixed abrasive diamond pellets (FADPs), which have been developed into fixed abrasive polishing. Cylinder pellets are bonded uniformly with a quantity of diamond abrasive, cemedin, and additive according to a specific ratio. The parameters of diamond pellets we used are listed in Table 2.2. The diamond granularity

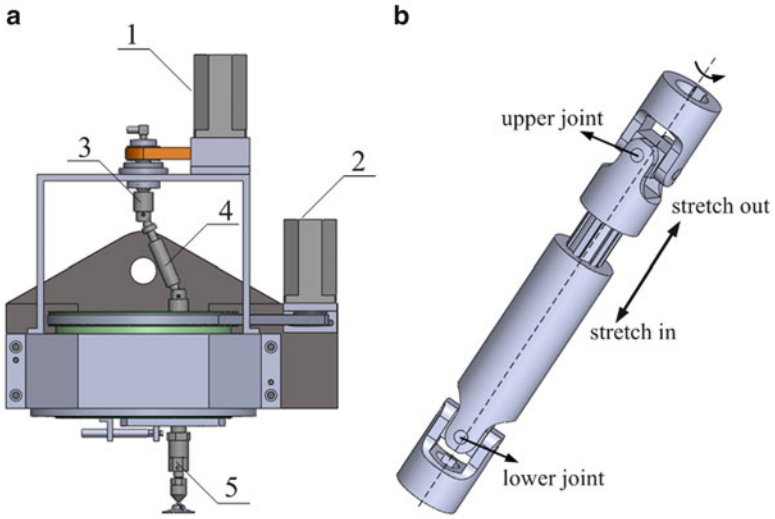

Fig. 2.8 Structure diagrams of (**a**) the fabrication unit; (**b**) the retractable universal joint

Table 2.2 Parameter list of fixed abrasive diamond pellets

Pellet kind	Diamond granularity (μm)	Bonding agent	Pellet diameter (mm)	Concentration (%)
W1.5	1.5	Resin	6	10
W3	3	Resin	6	10
W5	5	Resin	6	10
W17	17	Metal	6	10

varies from 1.5 to 17 μm, and all the concentrations of abrasive are 10 %. Resin and metal are adopted as cemedin. Continuously supplied deionized water is adopted as a coolant in all experiments. This structure characteristic brings in two advantages for TIFs.

1. *High stability*: Abrasive particles are uniformly distributed in the pellets, not just bonded in the outside surface. The thickness of pellets is 4 mm, and could be used for hundreds of hours. The external abrasives of pellets engender material removal by brittle fracture. When the external abrasives are worn down, sub-surface abrasives reach the top and keep removing material. This kind of removal feature guarantees the stable concentration distribution of abrasives, and then brings in highly stable material removal.
2. *High removal rate*: The abrasives are fixed on a cylinder rather than in the dissociative status, which could provide much larger shear force. Simultaneously, the ubiquitous splash phenomenon of abrasive slurry in loose abrasive polishing is avoided, which makes fixed abrasive polishing allow high speed (it is easy to achieve 1,000 rpm). These features certainly bring in a higher removal rate than loose abrasive.

Table 2.3 Fixed abrasive polishing pads with different distribution models

Model number	Sketch map	Optimized f	Optimized g	Optimized 3D-TIFs
1	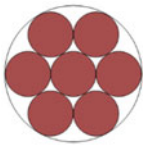	−3	0.8	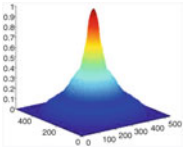
2	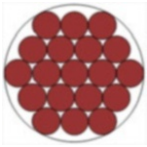	−3	0.8	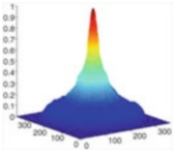
3	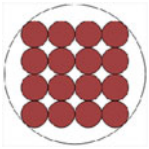	−3	0.7	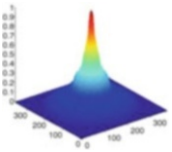
4	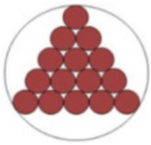	−5	0.7	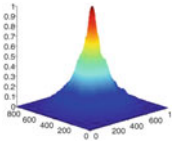
5	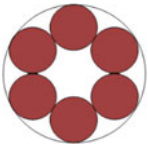	−5	0.6	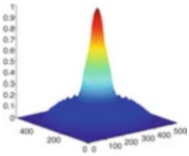
6	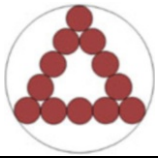	−4	0.6	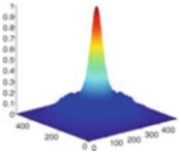

3D three-dimensional, *TIF* tool influence function

In the first step, the pellets are combined by hands into a polishing pad without a perfect flat or spherical surface, and could not be used for practical polishing. The next step, the pads should be modified to be a flat or spherical surface, by hand or machine, utilizing a flat or spherical steel plate to rub the pad rigidly. By this preprocess, the pad's surface could be coincident in curvature with SiC mirrors.

The polishing pads could be flexibly designed into different shapes, which provide us with different TIFs. To obtain the necessary TIF, we could make arbitrary changes in the amount of pellets, total aperture, position of the pellets and so on. According to the design experience of pitch pads, we design a mass of fixed abrasive polishing pads with different distribution models, such as circular, annular, square, triangle, and triangle annular, etc. These models are listed in Table 2.3. Some practical polishing pads are shown in Fig. 2.9.

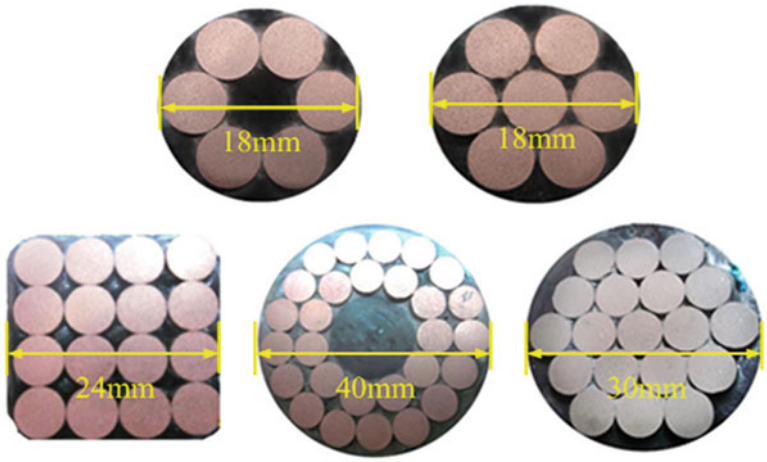

Fig. 2.9 Some practical polishing pads

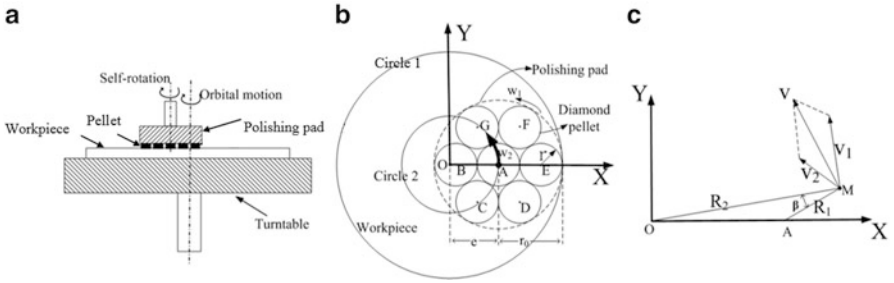

Fig. 2.10 The TIF model construction for fixed abrasive diamond pellet tool. *TIF* tool influence function

For fixed abrasive micro-grinding and polishing, the TIF model can be constructed as follows. As shown in Fig. 2.10, a calculation algorithm under the planetary motion model is established as follows.

In this model, the polishing pad moves in self-rotation and orbital motion. *Circle 1* is the polishing area in one orbital period, and *Circle 2* is the orbital trajectory. In the Cartesian coordinate *XOY*, point *O* is the orbital center. Points *A, B, C, D, E, F* and *G* represent every pellet's geometrical center, respectively—we call these center points of pellets (CPP). Obviously, point *A* also plays the role of the self-rotation center. The self-rotation angular speed of the polishing pad is w_1, and orbital angular speed is w_2. The radius of the single pellet is r, and the radius of the polishing pad is $r_0 = 3 \cdot r$. The acentric distance is e. In Fig. 2.10c, point M is an arbitrary point in the polishing area. The distance between M and O is R_2, and between M and A is R_1. v_1, v_2 represent self-rotation and orbital speed of M, respectively.

Two parameters are defined which are significant for the characteristics of TIFs. The first is the ratio between self-rotation and orbital annular speed, expressed as shown in Eq. (2.10). The other is the eccentricity, which could be expressed as the ratio between acentric distance and the pad's radius, which is presented in Eq. (2.11).

$$f = \frac{w_1}{w_2} \tag{2.10}$$

$$g = \frac{e}{r_0} \tag{2.11}$$

The orbital period is $T = 2\pi/w_2$. Divide the period T into n portions, one single portion $\Delta t = T/n$. Assume the initial position is the position as shown in Fig. 2.10, the TIF model construction. During the orbital period T, in a certain time of t, where $t = i \cdot \Delta t (i = 1, 2, 3 \ldots, n)$, the coordinates of CPPs during one period could be expressed as Eq. (2.12).

$$\left\{\begin{array}{l}
\left\{\begin{array}{l} X_A = e - e \cdot \left(1 - \cos\left(w_2 \cdot t\right)\right) \\ Y_A = e \cdot \sin\left(w_2 \cdot t\right) \end{array}\right. \\
\left\{\begin{array}{l} X_B = e - 2 \cdot r - e \cdot \left(1 - \cos\left(w_2 \cdot t\right)\right) + 2 \cdot r \cdot \left(1 - \cos\left(w_1 \cdot t\right)\right) \\ Y_B = 0 + e \cdot \sin\left(w_2 \cdot t\right) - 2 \cdot r \cdot \left(\sin\left(w_1 \cdot t\right)\right) \end{array}\right. \\
\left\{\begin{array}{l} X_C = e - r - e \cdot \left(1 - \cos\left(w_2 \cdot t\right)\right) + r - 2r \cdot \sin\left(\pi/6 - w_1 \cdot t\right) \\ Y_C = -3^{1/2} \cdot r + e \cdot \sin\left(w_2 \cdot t\right) - \left(2r \cdot \cos\left(\pi/6 - w_1 \cdot t\right) - 3^{1/2} \cdot r\right) \end{array}\right. \\
\left\{\begin{array}{l} X_D = e + r - e \cdot \left(1 - \cos\left(w_2 \cdot t\right)\right) + 2r \cdot \cos\left(\pi/3 - w_1 \cdot t\right) - r \\ Y_D = -3^{1/2} \cdot r + e \cdot \sin\left(w_2 \cdot t\right) + \left(3^{1/2} \cdot r - 2r \cdot \sin\left(\pi/3 - w_1 \cdot t\right)\right) \end{array}\right. \\
\left\{\begin{array}{l} X_E = e + 2 \cdot r - e \cdot \left(1 - \cos\left(w_2 \cdot t\right)\right) - 2 \cdot r \cdot \left(1 - \cos\left(w_1 \cdot t\right)\right) \\ Y_E = 0 + e \cdot \sin\left(w_2 \cdot t\right) + 2 \cdot r \cdot \left(\sin\left(w_1 \cdot t\right)\right) \end{array}\right. \\
\left\{\begin{array}{l} X_F = e + r - e \cdot \left(1 - \cos\left(w_2 \cdot t\right)\right) + 2r \cdot \sin\left(\pi/6 - w_1 \cdot t\right) - r \\ Y_F = 3^{1/2} \cdot r + e \cdot \sin\left(w_2 \cdot t\right) + \left(2r \cdot \cos\left(\pi/6 - w_1 \cdot t\right) - 3^{1/2} \cdot r\right) \end{array}\right. \\
\left\{\begin{array}{l} X_G = e - r - e \cdot \left(1 - \cos\left(w_2 \cdot t\right)\right) + r - 2r \cdot \cos\left(\pi/3 - w_1 \cdot t\right) \\ Y_G = 3^{1/2} \cdot r + e \cdot \sin\left(w_2 \cdot t\right) - \left(3^{1/2} \cdot r - 2r \cdot \sin\left(\pi/3 - w_1 \cdot t\right)\right) \end{array}\right.
\end{array}\right. \tag{2.12}$$

We can obtain the motion trajectory of every CPP through Eq. (2.12). During T, assume the total contiguous time between M and the polishing pad is t_M, initialize $t_M = 0$. In time t, we can easily obtain the length of line segments $\overline{MA}$, $\overline{MB}$, $\overline{MC}$, $\overline{MD}$, $\overline{ME}$, $\overline{MF}$, $\overline{MG}$, if they satisfy Eq. (2.13), then M and the polishing pad are contiguous in time t; in other words, t is a valid time segment, then $t_M = t_M + t$. Circulate every t to get t_M. The intersection angle between O and the circular arc path of M in the polishing pad is $2\alpha = 2 \cdot t_M/n \cdot \pi$. Relative speed between O and M could be expressed as Eq. (2.14).

$$\overline{MA} < r \left| \overline{MB} < r \right| \overline{MC} < r \left| \overline{MD} < r \right| \overline{ME} < r \left| \overline{MF} < r \right| \overline{MG} < r \tag{2.13}$$

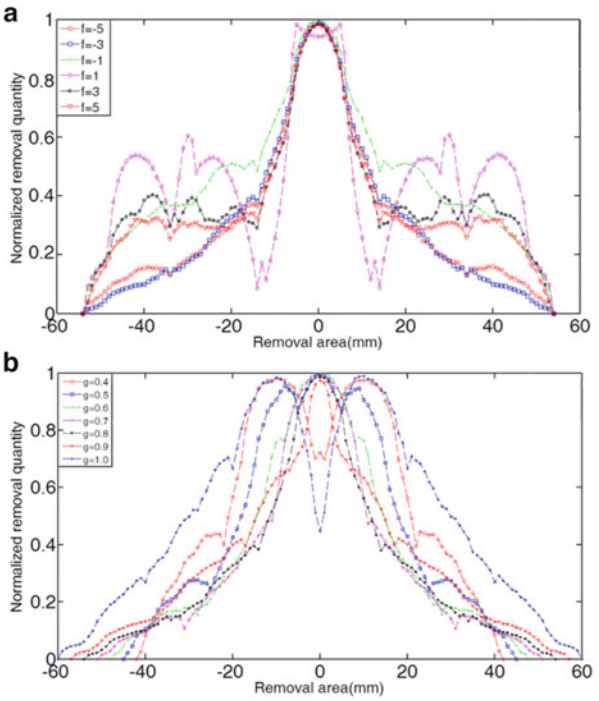

Fig. 2.11 (**a**) Different removal functions (RFs) under different speed ratios; (**b**) different RFs under different eccentricity ratios

$$\begin{aligned} |\boldsymbol{v}| &= |\boldsymbol{v}_1 + \boldsymbol{v}_2| \\ &= \left(v_1^2 + v_2^2 - 2v_1 v_2 \cos\beta\right)^{1/2} \\ &= \left(\left(R_1 w_1\right)^2 + \left(R_2 w_2\right)^2 - 2R_1 w_1 R_2 w_2 \cos\beta\right)^{1/2} \end{aligned} \tag{2.14}$$

Where: $\beta = \arccos\left(\frac{R_1^2+R_2^2-e^2}{2R_1R_2}\right)$, $R_2 = (R_1^2 + e^2 - 2R_1 e \cos\alpha)^{1/2}$.

The contiguous time of M is expressed as Eq. (2.15).

$$\mathrm{d}t = \mathrm{d}\alpha / w_2 \tag{2.15}$$

Combine Eqs. (2.14) and (2.15), and the Preston function, the TIF can be obtained by Eq. (2.16).

$$\mathrm{TIF}(r) = \mathrm{d}z = \int_{-\alpha}^{\alpha} K \cdot P \cdot v / w_2 \cdot \mathrm{d}\alpha \tag{2.16}$$

where TIF(r) is the tool influence function, K is the Preston constant, P is the pressure between the polishing pad and workpiece, and v is the relative speed between the polishing pad and workpiece in M.

The theoretical TIFs under different parameters are shown in Fig. 2.11. Figure 2.11a represents different TIFs under different speed ratios while the

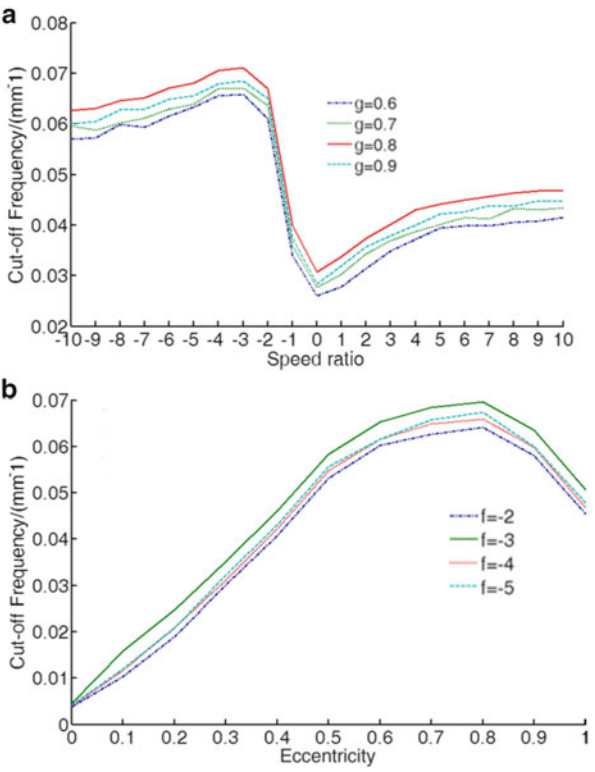

Fig. 2.12 Cutoff frequency about f and g

eccentricity ratio $g = 0.8$. Because of the desire for higher center removal rate, the optimized speed ratio is $f = -3$ or $f = -5$. Figure 2.11b shows different TIFs under different eccentricity ratios while speed ratio $f = -3$, we can find that $g = 0.7$ and $g = 0.8$ may be optimized selections.

2.3.1.2 Analysis and Optimization

Take model 1 in Table 2.3 for example, the cutoff frequency about f and g is calculated and plotted, respectively, in Fig. 2.12. Figure 2.12a indicates the cutoff frequency curves of $g = 0.6$, $g = 0.7$, $g = 0.8$, $g = 0.9$, while the speed ratio varies from -10 to 10 by 1. When the speed ratio is negative, the cutoff frequency shows much higher than positive speed ratio. For higher cutoff frequency, $f = -3$ could be taken as the best speed ratio from these curves. Figure 2.12b reveals the cutoff frequency curves of $f = -2$, $f = -3$, $f = -4$, $f = -5$, while eccentricity varies from 0 to 1.0 by 0.1. Here, we set the scale of all the TIFs as 40 mm. The maximum cutoff frequency appears in $g = 0.8$.

Therefore, we generally take $f = -3$ and $g = 0.8$ as the optimized parameters. They are generally coincident to the prediction in the above analysis.

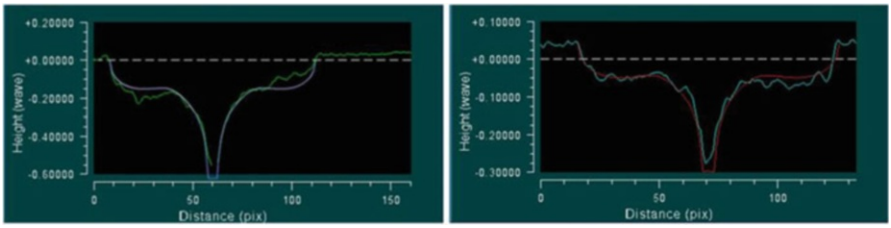

Fig. 2.13 Contrast of practical removal profile and emulational profile

2.3.1.3 Experimental Validation

Experiments are conducted to validate the effectiveness of the model on forecasting the removal profile of small-tool polishing. Detailed parameters are concluded as follows: the optical segment is a 200 mm SiC, which was per-polished to be a fine plane surface. The experiments adopted 10 weight percent (wt%) CeO_2, press kept 30 N. Tool size was 30 mm, and the polishing material was 4# pitch. The eccentric distance was 12 mm, and the orbital and spinning velocity were 60 rpm and 480 rpm, respectively. The experimental result was measured by Zygo GPI and shown in Fig. 2.13 (*left*). We find that the profile of TIF is highly identical to the emulational profile. The second polishing process decreased the spinning velocity to 300 rpm, and obtained results as shown in Fig. 2.13 (*right*), which also has high similarity.

We performed a series of experiments on reaction-bonded SiC mirrors to validate the algorithm and optimized parameters; results of TIFs of model 1 and 5 are presented in Fig. 2.14. Corresponding experimental parameters are listed in Table 2.4.

As shown in Fig. 2.14, the TIFs with a high removal center are obtained, which could help raise the convergence rate in a polishing run. The coincidence of profile between experimental and theoretical TIFs is generally satisfactory. The small difference is mainly caused by the unsuitability between the optical surfaces and polishing pads, which inevitably exists. These processes validate the effectiveness of the proposed algorithm.

A polishing pad of model 5 with pellets of diamond granularity 3 μm is used to validate the stability of TIFs as usage time increases. The experimental parameters are listed in Table 2.5 and the experimental results are shown in Fig. 2.15.

In Fig. 2.15a, the upper removal shape (shown as I) is experiment 1, in which the usage time of polishing pads is $t = 0 - 10$ min. The lower removal shape (shown as II) is experiment 2, whose usage time is $t = 300 - 310$ min. During the usage time from 10 to 300 min, the pad is used to polish another SiC workpiece. In Fig. 2.15b, the left curve is a 2D profile of experiment 1, and the right curve is a 2D profile of experiment 2. We could find the result shows high stability both in profile shape and peak removal magnitude as tool usage time increases. This means, during

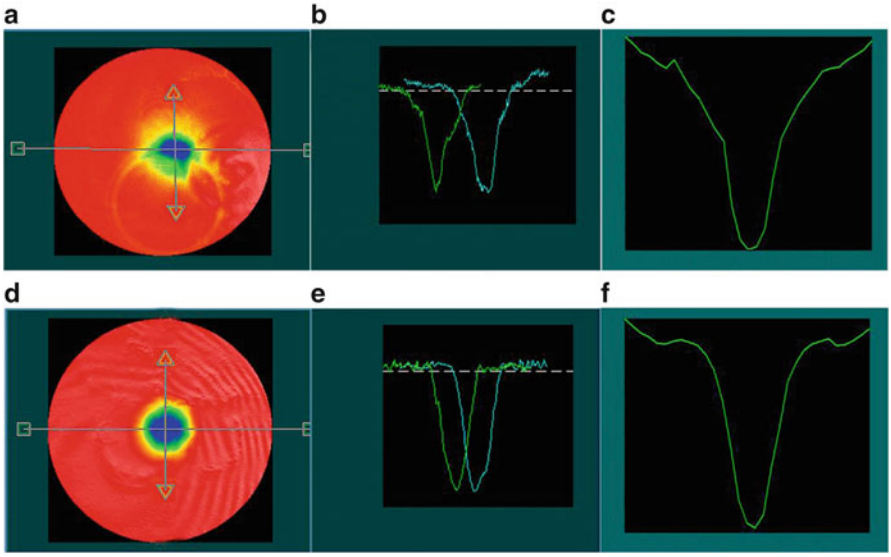

Fig. 2.14 Results of TIFs of models 1 and 5. *TIFs* tool influence functions

Table 2.4 Corresponding experimental parameter of models 1 and 5

Number	Model	Pellets	f	g	Pressure (N)	Time (min)
1	1	W3	−3	0.8	30	10
2	5	W3	−3	0.8	30	10

Table 2.5 Experimental parameters for tool influence function stability

Remarks	Usage time (min)	f	g	Pressure (N)
Experiment 1	0–10	6	0.8	20
Experiment 2	300–310	6	0.8	20

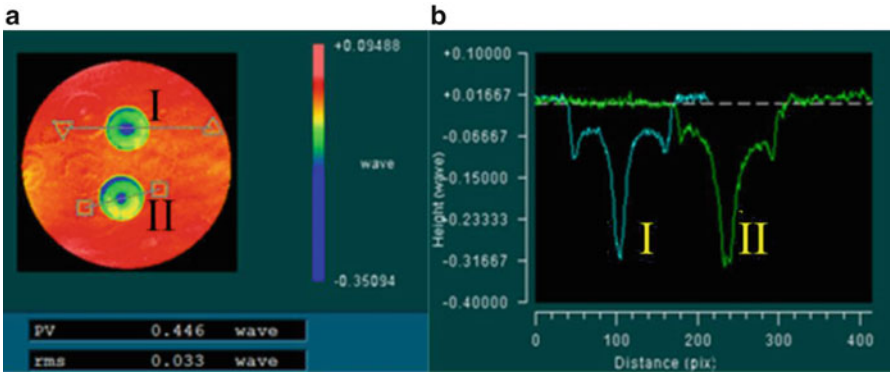

Fig. 2.15 (**a**) *Top* view removal shape; (**b**) *left* curve is a 2D profile of experiment 1, and the *right* curve is a 2D profile of experiment 2. *2D* two-dimensional

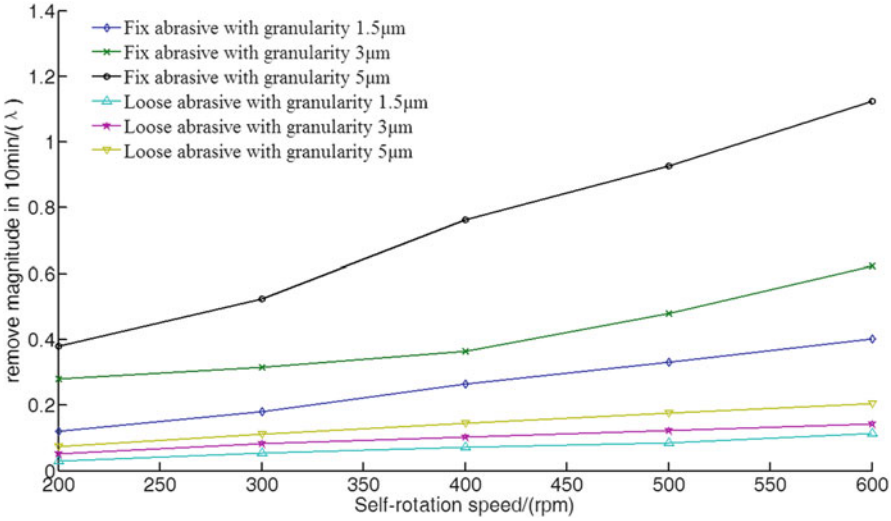

Fig. 2.16 Results of ten experiments

Table 2.6 Conditions of experiments for removal rate

Number	Polishing pads	Granularity (μm)	Self-rotation speed (rpm)	f	g	$F(N)$
1	Diamond pellets	1.5	200–600	−3	0.8	30
2	Diamond pellets	3	200–600	−3	0.8	30
3	Diamond pellets	5	200–600	−3	0.8	30
4	Pitch + diamond abrasive	1.5	200–600	−3	0.8	30
5	Pitch + diamond abrasive	3	200–600	−3	0.8	30
6	Pitch + diamond abrasive	5	200–600	−3	0.8	30

rpm revolutions per minute

a relatively long polishing time (5 h or more), the fixed abrasive could provide highly stable TIFs for the polishing of SiC mirrors.

Tens of experiments are conducted to compare the removal rate of loose abrasive and fixed abrasive polishing. The results are plotted in Fig. 2.16. Table 2.6 lists the conditions of experiments. Experiments 1–3 are fixed abrasive polishing with granularity of 1.5, 3, 5 μm, respectively, and experiments 4–6 use pitch pad and diamond loose abrasives of 1.5, 3, 5 μm, respectively. In Fig. 2.16, every experiment includes five portions, whose self-rotation speed varies from 200 to 600 rpm. As an example, when the self-rotation speed is 500 rpm, and with 5 μm granularity, the loose abrasive removal magnitude in 10 min is 0.176 λ, and fixed abrasive is 0.926 λ, which could provide more than five times the removal rate. For other experimental parameters, fixed abrasive could generally achieve a removal rate

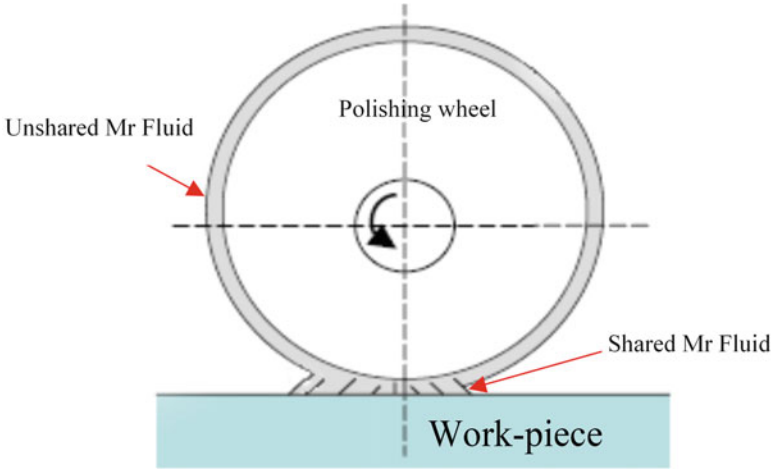

Fig. 2.17 Basic principle of MR fluid-assistive polishing. *MR* magnetorheological

about five times more than the loose abrasive, which could help save a great deal of fabrication time.

2.3.2 Magnetorheological Finishing System

2.3.2.1 Model Construction

Magnetorheological (MR) fluids are composed of small magnetic particles in disperse phase suspended in non-conducting carrier liquids. Under the effect of magnetic field, the magnetic particles are polarized and organized into chains or ribbons of particles. As such, the structure and rheological properties of MR fluids, such as viscosity and stress, can be dramatically altered. It normally takes only milliseconds for MR fluid passing through a magnetic field to stiffen up, and then return to its original state upon exiting, again in milliseconds. The phenomenon can thus be utilized for sub-aperture polishing of optical surfaces with the mixing of ultra-fine abrasive (non-magnetic) particles to the fluid. In this regard, Cheng et al. [4, 5] designed a wheel-tool for MR fluid-assistive polishing. As shown in Fig. 2.17, the portion of magnetically stiffened fluids becomes a polishing tool at the region of closest separation between the tool and the workpiece, where the fluid ribbon is squeezed from about 2 mm to 1 mm in thickness. As generated, the resulting sub-aperture tool has the advantage of producing significant shear stress and polishing pressure while automatically conforming closely to the local curvature being polished.

One precondition for successful MR polishing is the generation of suitable gradient of magnetic field by the wheel tool (Fig. 2.17). Researchers have proposed

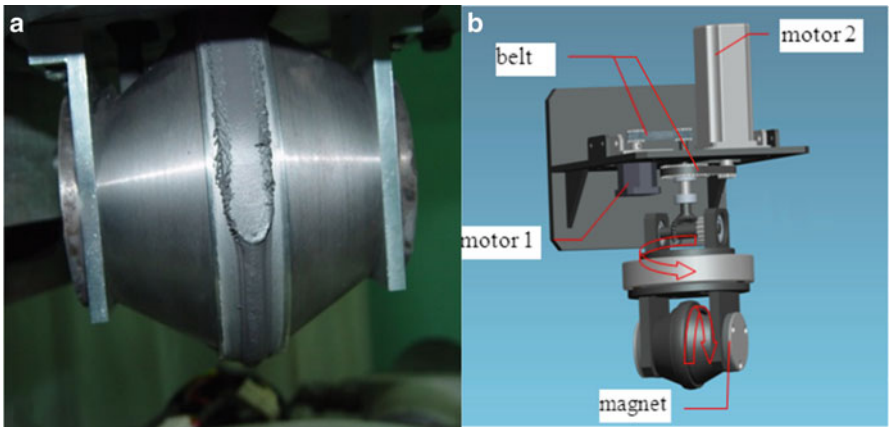

Fig. 2.18 (**a**) Actual wheel tool with workpiece; (**b**) main components of the tool design

various designs, e.g., Golini [6] and Cheng et al. [7], and conducted experiments validating their polishing performance. The previous works, however, all adopted tools that rotate about only one axis (the self-rotating axis). Their emphases were focused on testing the MR processes with different materials and studying the resulting performance. Little work was reported on using other wheel-tool design and understanding the effects of process parameters on MR polishing, analytically or experimentally.

The tool we designed adopts a two-axis wheel-shaped polishing tool, as shown in Fig. 2.18, for analysis and experimentation. Figure 2.18a shows the picture of the actual hardware and Fig. 2.18b depicts the main components of the setup. During MR polishing, the wheel tool is driven by motor 1 to rotate (with angular speed w_2) about its self-rotating axis through a belt and bevel gear setup, and at the same time by motor 2 to rotate (with angular speed w_1) about the co-rotating axis. Figure 2.19 shows the internal structure underneath the tool cover and the magnetic fields from the tool design. Referring to Fig. 2.19a, B1–B2 is a pair of ring magnets arranged symmetrically on the two sides of the wheel tool. The orientation is such that the tool's self-rotating axis is normal to the ring magnets at their centers. A1–A2 is a pair of rectangular magnets located near the bottom of the tool cover at close distance to the disc inside. The disc is an 'I' shaped wheel made of non-conducting material to carry MR fluids, and rotates about the self-rotating axis. The design has A1–A2 producing stronger magnetic intensity than B1–B2. The magnetic field lines around the disc can be determined from theory, as shown in the blue dashed lines in Fig. 2.19a. The two magnetic fields from A1–A2 and B1–B2 overlap at the bottom of the disc, resulting in a localized magnetic field with stronger intensity on top of a weaker field that is more broadly distributed over the disc surface. At the top apex of the disc, in particular, the field has minimum intensity. This physical description is verified by Fig. 2.19b, which shows the magnetic field lines simulated using finite element analysis. Note that for enhanced

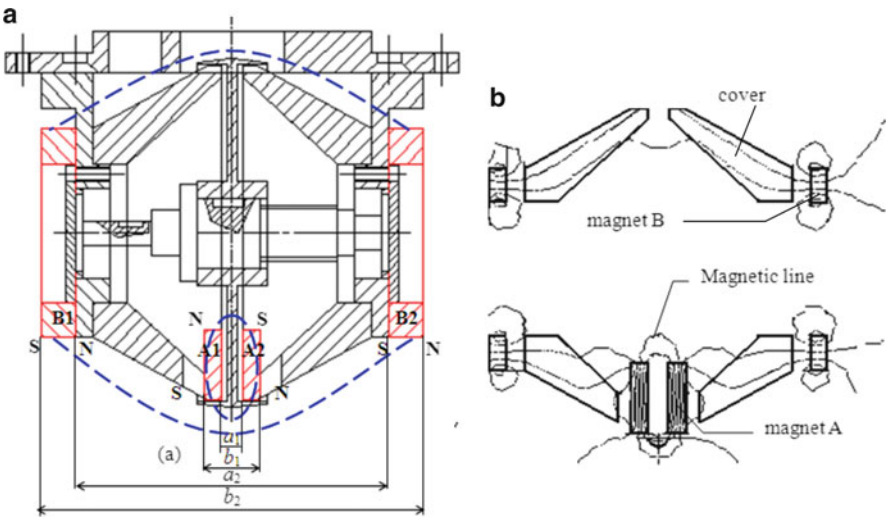

Fig. 2.19 (**a**) Internal structure and magnet distribution of the wheel tool; (**b**) magnetic field lines generated by finite element analysis (FEA) methods

polishing, the overall magnetic field should transverse the working gap between the polishing wheel and the workpiece in a direction as perpendicular to the workpiece surface as possible.

During actual polishing, the workpiece would sit on top of a turntable rotating at a relatively slow speed (to w_1 and w_2). MR fluid ribbon adhering to the surface of the wheel disc is transported into the gap between the disc surface and the workpiece. Under the action of the double magnetic fields, the stiffened fluid region forms a transient polishing zone or spot on the workpiece surface. Surface material within this polishing spot is removed by the self-rotating motion. The role of the co-rotating motion is to continually re-orient the direction of the self-rotation motion to smooth out any angular preference in the polishing spot. Moreover, once the fluid ribbon is transported outside the gap by the disc's self-rotation, it tends to disband and lose the ability to carry the abrasive particles because of reduction in the magnetic field intensity. The role of the magnetic field B1–B2, although at weaker intensity, is to maintain the shape of the ribbon to a certain extent, and to help with the loosening, recombination, and replenishing of the abrasive particles.

Polishing is a complex process and both relative velocity and pressure between the tool and the workpiece are important factors to consider. As the tool travels over the workpiece surface, the material can be obtained from the convolution of the material removal function with the dwell time along the polishing path. The material removal function is given by the Preston function discussed in Chap. 1.

The wheel tool's relative velocity is a combination of its self-rotation and co-rotation motions. The relatively slower self-rotation of the turntable on which the workpiece is sitting is omitted. Figure 2.20 depicts the transient polishing spot

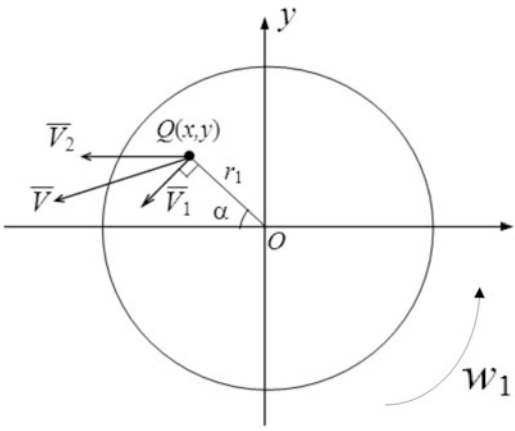

Fig. 2.20 Polishing spot on workpiece indicating relative velocity due to wheel tool rotations

mentioned above on the workpiece surface. The relative velocity at an arbitrary point $Q(x,y)$ inside the polishing spot can be expressed as

$$\vec{V} = \begin{cases} \vec{V}_2 + \vec{V}_1 \\ w_1 r_1 \rightarrow \vec{V}_1 \\ w_2 r \rightarrow \vec{V}_2 \end{cases} \tag{2.17}$$

where $\overline{V}_1$ and $\overline{V}_2$ are the linear velocities due to the co-rotation and self-rotation motion, respectively, at point Q, r_1 is the distance from point Q to the center O of the polishing spot, and r is the wheel-disc's semi-diameter. Note that O here is also the center of the co-rotation motion—the co-rotation axis would be the normal to the polishing spot at this point. Thus,

$$V = \sqrt{(w_1 r_1)^2 + (w_2 r)^2 - 2 w_1 w_2 r_1 r \cos\left(\frac{\pi}{2} + \alpha\right)} \tag{2.18}$$

The normal pressure P inside the polishing spot is a very complicated quantity. It can be divided into two parts: the hydrodynamic pressure P_h and the magnetic pressure P_m, i.e.,

$$P = (P_h + P_m) \cdot \frac{\sqrt{r^2 - x^2}}{r} \tag{2.19}$$

The multiplicative factor in Eq. (2.19) serves to convert the pressure exerted along the radial direction of the disc to the normal direction of the polishing spot. As the MR fluid is incompressible, its contribution to P_h can be ignored. P_h can hence be simplified, as shown by Chi et al. [8]:

$$P_h = \frac{2\eta V}{\left(d + \frac{x^2}{2r}\right)^2} \tag{2.20}$$

where d is the minimum gap between the bottom of the wheel disc and the surface of the workpiece, and η is the working viscosity of the MR fluid during the process.

The magnetic fields generated by the wheel tool in Fig. 2.19 can be derived roughly from the theory. Approximating the magnet arrangement for both A1–A2 and B1–B2 as parallel plates, the distribution of the magnetic intensity H in-between A1–A2 and B1–B2 can be expressed as,

$$\begin{cases} H = \sum_{n=1}^{\infty} - A_n \cos(\beta_n x) e^{-\beta_n y i} + \sum_{n=1}^{\infty} A_n \sin(\beta_n x) e^{-\beta_n y j} \\ A_n = K_n \beta_n = \dfrac{2B_g \sin\left(\beta_n \dfrac{a}{2}\right)}{\pi(2n-1)\mu_0} \\ \beta_n = \dfrac{2n-1}{b}\pi \\ K_n = \dfrac{2b \cdot B_g \cdot \sin\left(\beta_n \dfrac{a}{2}\right)}{\pi^2 \cdot (2n-1)^2 \cdot \mu_0}, \quad n = 1, 2, 3 \ldots \end{cases} \tag{2.21}$$

where n is the iterative order number, A_n, β_n, and K_n are the corresponding coefficients, B_g is magnetic induction intensity, μ_0 is the permeability of vacuum, and a is the inner distance and b the outer distance between the two magnets in A1–A2 or B1–B2, as the case may be. Consider then the interaction force between aggregated magnetic particles under the action of the magnetic field. A magnetic particle, e.g. a spherical carbonyl iron (CI) particle, of radius R and magnetic permeability μ_p will have a magnetic moment of

$$m = 4\pi\mu_0\mu_\mathrm{f} R^3 \frac{\mu_\mathrm{p} - \mu_\mathrm{f}}{\mu_\mathrm{p} + 2\mu_\mathrm{f}} H \tag{2.22}$$

where μ_f is the magnetic permeability of the carrier liquid. Let ϕ be the fractional volume of magnetic particles in the MR fluid, the magnetic pressure P_m is hence, approximately,

$$P_m = \phi \int_0^H \frac{m}{\frac{4}{3}\pi R^3} \mathrm{d}H = 3\phi\mu_0\mu_\mathrm{f} \frac{\mu_\mathrm{p} - \mu_\mathrm{f}}{\mu_\mathrm{p} + 2\mu_\mathrm{f}} \int_0^H H \mathrm{d}H \tag{2.23}$$

Table 2.7 Design and operating parameters of the two-axis wheel tool

Parameter	Value
Radius of carbonyl iron particles R (μm)	1–5
Volume fraction of carbonyl iron particles in fluid ϕ (%)	20–40
Volume fraction of CeO_2 particles in fluid ϕ (%)	3–8
Volume fraction of water in fluid ϕ (%)	50–75
Magnetic induction intensity of A1–A2 B_{g1} (T)	0.99
Magnetic induction intensity of B1–B2 B_{g2} (T)	0.35
Permeability of vacuum μ_0 (H/m)	$4\pi \times 10^{-7}$
Magnetic permeability of host fluid μ_f (H/m)	$4\pi \times 10^{-7}$
Magnetic permeability of magnetic particles μ_p (H/m)	2×10^{-3}
Distance between two insides of A1–A2 a_1 (mm)	6
Distance between two outsides of A1–A2 b_1 (mm)	26
Distance between two insides of B1–B2 a_2 (mm)	120
Distance between two outsides of B1–B2 b_2 (mm)	140
Wheel-disc's semi-diameter r (mm)	43
Gap between disc's bottom and the workpiece d (mm)	1–2.5
Co-rotational speed of the tool w_1 (rpm)	100
Self-rotational speed of the tool w_2 (rpm)	0–200

For the tool design supporting dual magnetic fields, P_m is composed of P_{m1} and P_{m2} individually produced by the magnets A1–A2 and B1–B2, i.e.

$$P_m = P_{m1} + P_{m2} \tag{2.24}$$

Table 2.7 lists the design and operating parameters of the two-axis tool adopted for the present study. Based on the values given, hydrodynamic pressure and magnetic pressure are computed at varying distances from the center point O of the polishing spot. They are plotted in Fig. 2.21, assuming a typical polishing spot of 5 mm radius. The magnetic pressure is about six orders of magnitude smaller than those of hydrodynamic pressure. This points to a simplification of the relative pressure P as,

$$P \approx P_h \cdot \frac{\sqrt{r^2 - x^2}}{r} = \frac{2\eta V}{\left(d + \frac{x^2}{2r}\right)^2} \cdot \frac{\sqrt{r^2 - x^2}}{r} \tag{2.25}$$

Accordingly, material removal is directly related to such process parameters as the minimum gap d between the bottom of the wheel disc and the surface of the workpiece, the relative velocity V, and the working viscosity of the MR fluid η. The main effect of the applied magnetic field is not on P_m but on increasing the viscosity η of the polishing process. Actually, the working viscosity is affected by both the magnetic field intensity and fractional volumes of different components of the fluid. In this regard, the field intensity to make MR fluid stiff enough to support the polishing process has been investigated by Cheng et al. [4, 7]. The following efforts will be devoted to studying the fractional volume composition of MR fluid, ensuring that a sufficient level of magnetic intensity is being applied.

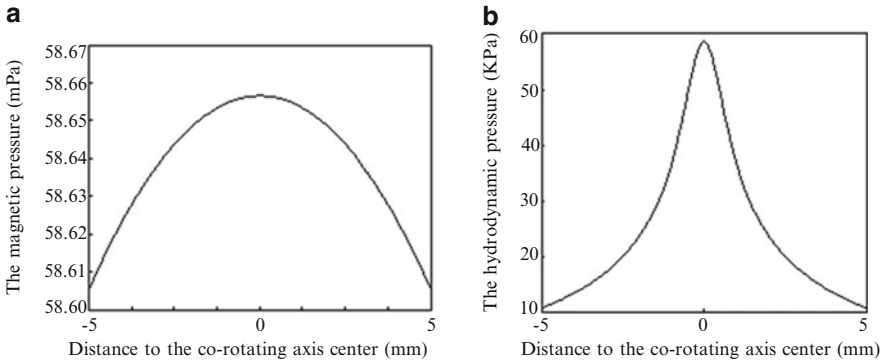

Fig. 2.21 (**a**) Plot of magnetic pressure and (**b**) hydrodynamic pressure as function of distance to the center of the polishing spot (Reproduced from Cheng et al. [5])

Table 2.8 Experiments to study material removal

Time (min)	w_2 (rpm)	d (mm)	ϕ of CI (%)	ϕ of CeO_2 (%)	ϕ of water (%)
10–60	150	1	33	6	57
30	0–200	1	33	6	57
30	150	1–2.5	33	6	57
30	150	1	20–40	6	57
30	150	1	33	3–8	57
30	150	1	33	6	50–75

rpm revolutions per minute, *CI* carbonyl iron

2.3.2.2 Experimental Validation

Experiments were conducted first to validate the general performance of the two-axis wheel tool and also to test out the best MR fluid composition for material removal. The experimental settings are listed in Table 2.8 and the results given in Fig. 2.22. A K9 glass parabolic lens of 60 mm diameter was used as the workpiece.

Figure 2.22a shows the increased amount of material being removed as a function of the polishing time. Figures 2.22b–f further show the maximum removal rate attained upon the varying of different design and process parameters. These plots show that maximum removal rate increases with the tool's self-rotational speed, the fractional volume of magnetic particle CI and abrasive particle CeO_2 in the MR fluid, and decreases with the increasing of the gap between the disc and the workpiece and the fractional volume of host water in MR fluid. For higher mixing ratio of abrasive particles in the fluid, more abrasives would be engaged in polishing within a unit time and hence a faster rate of material removal. On the other hand, when too much CI is mixed into the MR fluid, the fluidity would deteriorate and small clumps would accumulate under the action of the magnetic field, resulting in unsatisfactory polishing conditions. According to the experimental results, a tool

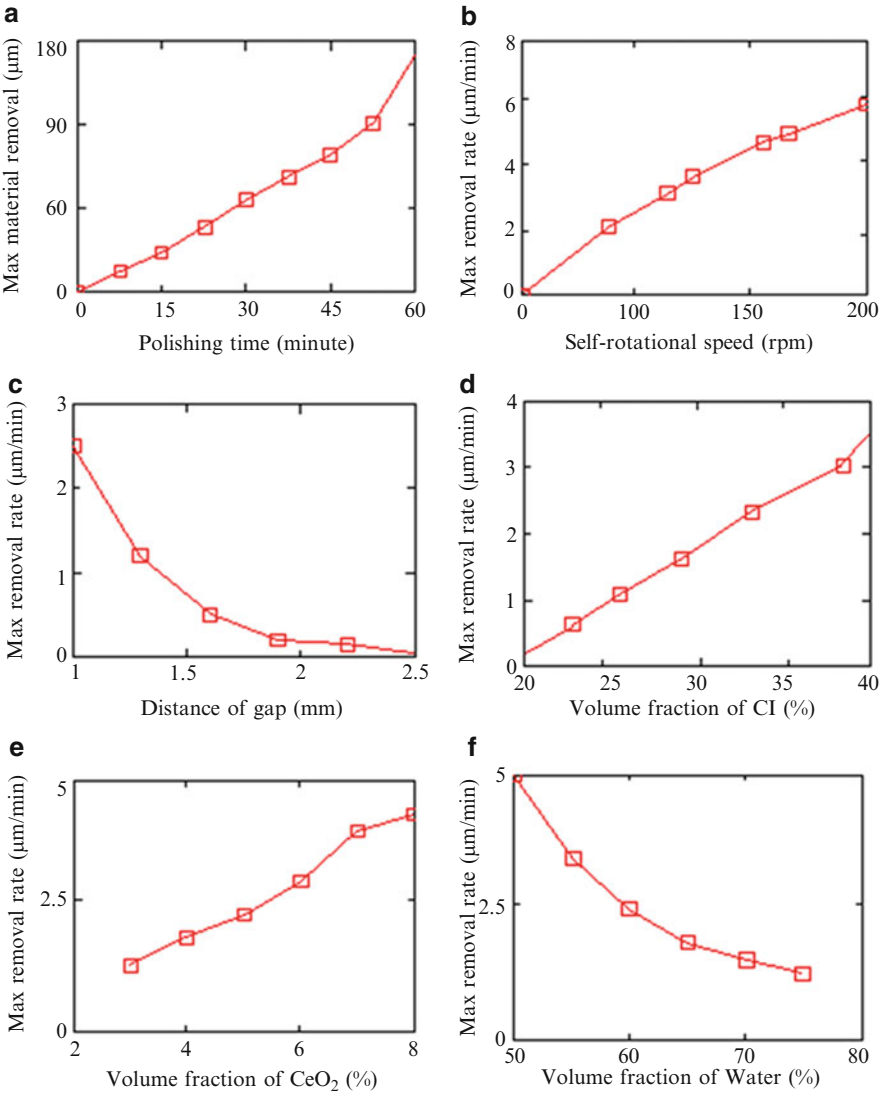

Fig. 2.22 Experimental results for the maximum material removal and the rate of versus (VS). (**a**) Polishing time; (**b**) the tool's self-rotational speed; (**c**) gap between the tool-disc's bottom and the workpiece; (**d**) volume fraction of CI; (**e**) volume fraction of CeO_2; (**f**) volume fraction of host fluid water in the MR fluid. *CI* carbonyl iron, *MR* magnetorheological (Reproduced from Cheng et al. [5])

speed ranging from 50 to 180 rpm, a gap distance ranging from 1 to 2 mm, and an MR fluid with 33 % CI, 57 % water, 6 % CeO_2, and 4 % stabilizing agent were deemed to provide the best removal performance.

Figure 2.23 shows the polishing performance on the K9 glass lens, taking into consideration the above findings. In Fig. 2.23a, it is easy to observe that the removal

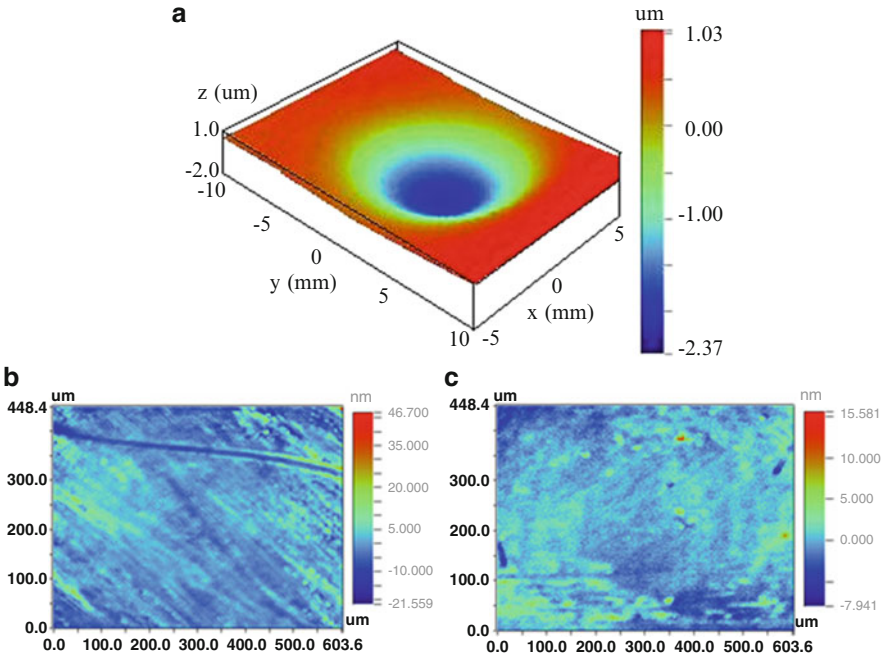

Fig. 2.23 3D profile of polishing spot (**a**) and surface roughness microstructure measured by a Wyko interferometer showing (**b**) initial Roughness average (Ra) = 3.8 nm, and (**c**) Roughness average (Ra) = 1.2 nm after 10 min of pre-polishing. *3D* three-dimensional (Reproduced from Cheng et al. [5])

function spot with a higher central peak would result in successful polishing. To achieve a smooth surface, we divide the process into pre-polishing and fine polishing stages. The pre-polishing uses a gap distance of 1 mm and a self-rotational speed of 180 rpm, whereas fine polishing resets the gap distance to between 1.5 and 2 mm while keeping the same self-rotation speed. It can be seen that surface roughness is reduced from Ra = 3.8 nm in Fig. 2.23b to Ra = 1.2 nm in Fig. 2.23c after 10 min of pre-polishing. The very apparent marks in Fig. 2.23b are readily smoothed out. The results confirm the overall effectiveness of the experimental process parameters and MR fluid composition in the quality polishing of optical surfaces using a two-axis wheel tool.

2.3.3 Magnetorheological Jet Polishing System

2.3.3.1 Model Constructions

The design of the jet tool with the electric current and steady jet is more complex in the eccentric rotation system than in the traditional system. Cheng et al. [9] reports a polishing tool with eccentric rotation motion, as shown in Fig. 2.24. This

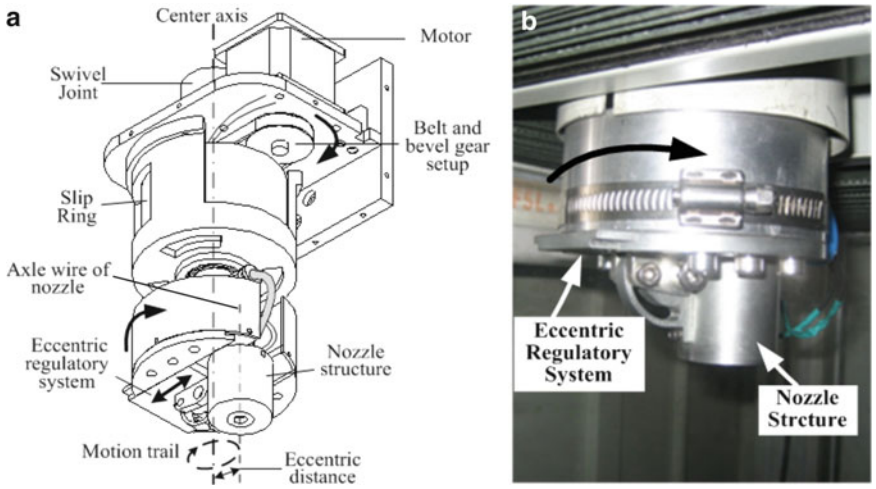

Fig. 2.24 Experimental setup. (**a**) computer aided design (CAD) of polishing setup; (**b**) main components of actual hardware

polishing tool can implement eccentric rotation motion mainly due to the utilization of eccentric regulatory system, swivel joint and slip ring. During the polishing process, the eccentric distance which depends on the diameter of the nozzle, is regulated by the eccentric regulatory system at first. This tool is then moved by high-precision machine to the target location on the glass for polishing. After that, eccentric regulatory system and nozzle structure will be driven to rotate around the center axis by the motor through belt and bevel gear setup. Meanwhile, the steady current will be transmitted from the external system to the coil via the slip ring, and the function of the swivel joint is similar to the slip ring, which transmits the continuous slurry from the external system to the nozzle (the coil and nozzle are in the interior of nozzle structure). The round jet is magnetized by the magnetic coil when it flows out of the nozzle. Therefore, the motion trail of the jet is circular, in particular, and its center is in the center axis as shown in Fig. 2.24.

According to the studies of Tricard et al. [10] and Kordonski et al. [11], the removal rate R at one point (x, y) can be expressed as below

$$R = kpv = k\frac{f}{\mu S}v = k\frac{D}{\mu} \tag{2.26}$$

where k is a constant parameter but depends on surface chemistry, workpiece material properties, and the slurry, etc., p is the normal pressure, v is the relative velocity between abrasives and the workpiece, f is the frictional force between the workpiece and the polishing lap, S is polishing zone, μ is the coefficient of friction, and D is the rate of work carried out at the surface.

When the MR jet passes beyond the magnetic field and is directed vertically towards the workpiece, the remanence declines fast and becomes very weak when

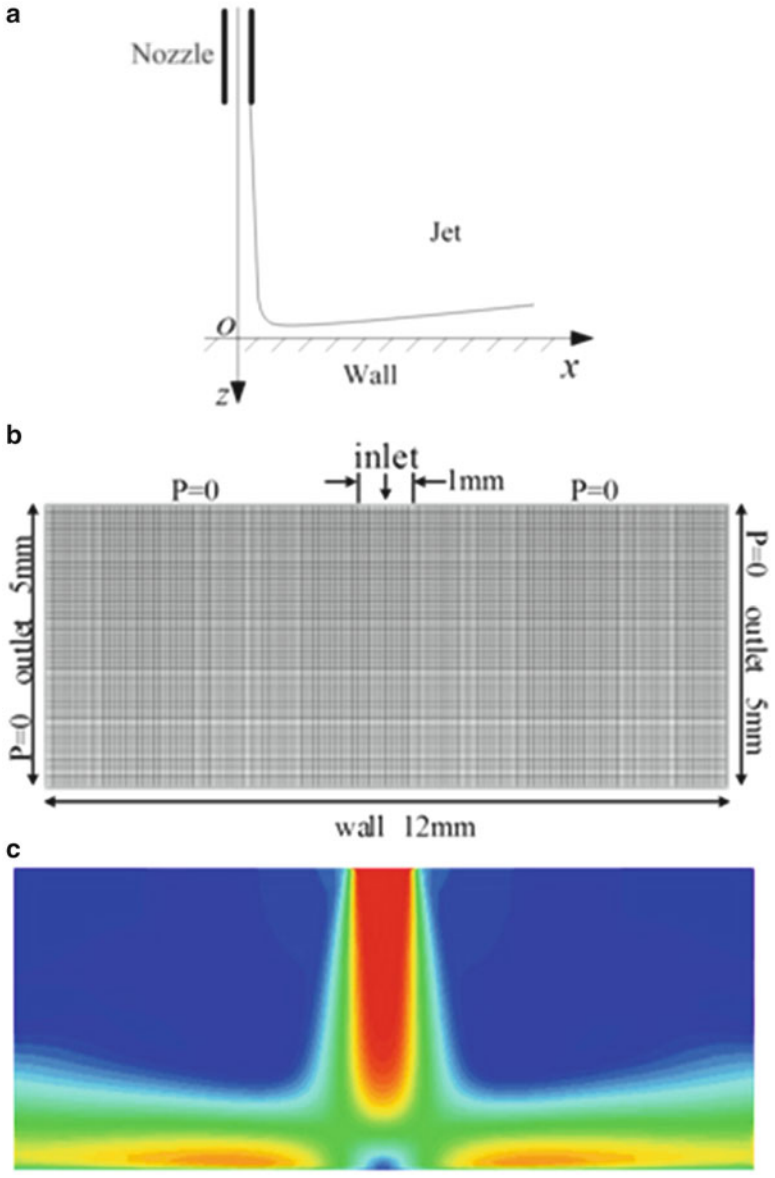

Fig. 2.25 Free impinging jet model. (**a**) Simple mode of jet; (**b**) mesh and boundary of the model; (**c**) simulation result with the jet velocity 20 m/s and nozzle diameter 1 mm

the jet impinges on the workpiece. Hence, the magnetic field can be ignored at the impingement area on the workpiece, and an assumption is made that the free impinging jet polishing theory (proposed by Becker et al. [12]) can be employed approximately nearby the workpiece where the jet remains coherent. A typical jet polishing model is shown in Fig. 2.25. The coherent jet hits the surface vertically.

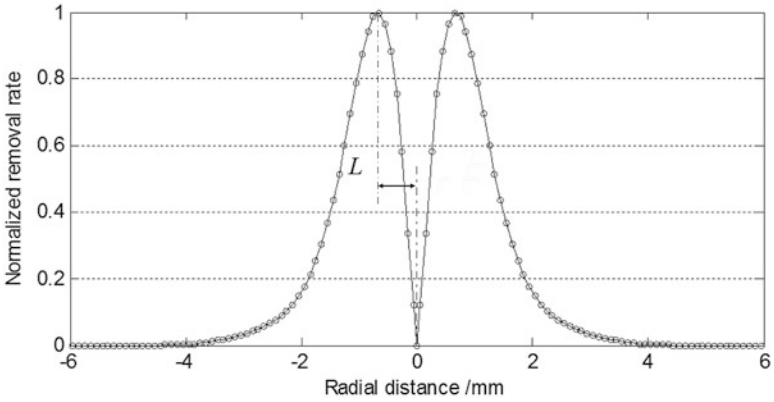

Fig. 2.26 Removal rate of normal jet polishing

Subsequently, the slurry is streaming radially away from the central point O along the surface, as seen in Fig. 2.25a. The normalized radial distribution of the rate of work done at the surface is calculated using commercially available Computational Fluid Dynamics (CFD) software. The model is shown in Fig. 2.25b. The diameter of the nozzle equals 1 mm, mesh area is 5 mm $\times$ 12 mm, and mesh size is 0.1 mm $\times$ 0.1 mm. The slurry jets form the inlet with a velocity of 20 m/s and flow out from the outlet (the boundary condition P equals 0, which is relative to the standard atmosphere), and the bottom of the mesh area is the wall. The velocity field distribution is shown in Fig. 2.25c.

By calculation through Eq. (2.26), the removal distribution with 1 mm diameter of the nozzle is exhibited in Fig. 2.26. The emulational result has a W-shaped profile across the polishing area. L is the horizontal distance between the peak and its adjacent valley, and it is about 0.7 mm when the diameter of the nozzle is 1 mm (see Fig. 2.26).

As seen in Fig. 2.26, the normal jet polishing does not have the deepest removal at the center. In order to obtain the Gaussian-like removal character, the eccentric rotation motion jet model is adopted. Figure 2.27 shows the polishing model with eccentric rotation motion. Figure 2.27a shows the principle of motion. The MR fluid with abrasives is delivered to the nozzle and directed vertically towards the workpiece. At the same time, nozzle spins on the axis of rotation with small eccentric distance e and angular-velocity. Figure 2.27b shows an arbitrary point p (r_2,θ_1) on the workpiece. r is the radius of the footprint around the central point o. The footprint of the normal jet along the trajectories forms a rotary symmetrical shape with the radius r_1 around the center of the rotation axis o_1. The distance between o_1 and o is eccentric distance e. The angle formed by $\overline{po}$ (length is d) and the X-axis is θ. When the jet rotates along the trajectories in a period, the effective range of polishing on p is $2\theta'$.

As shown in Fig. 2.28, rotation velocity vector $\mathbf{v}_e$ and fluid velocity vector $\mathbf{v}_l$ are introduced to describe relative velocity of the eccentric rotation motion mode on the

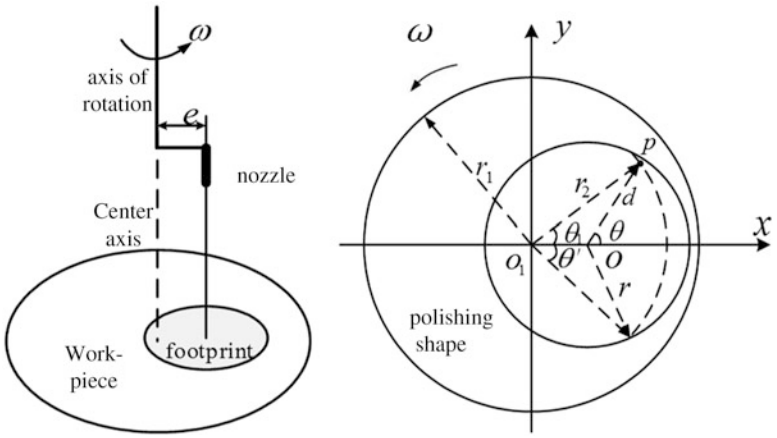

Fig. 2.27 Model of jet polishing with eccentric rotation motion. (**a**) Principle of motion; (**b**) polishing spot *p* on workpiece

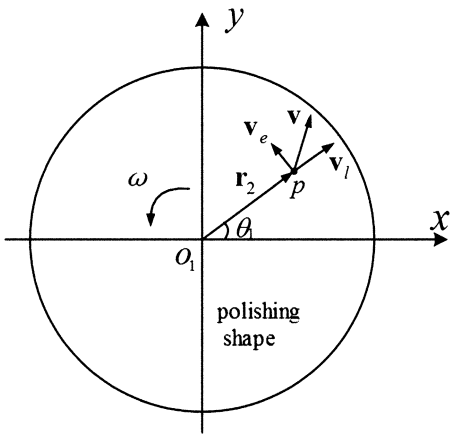

Fig. 2.28 Relative velocity of the eccentric rotation motion model

workpiece surface. The relative velocity at the point $p(\mathbf{r}_2,\theta_1)$ inside the polishing spot can be expressed as

$$\begin{cases} \mathbf{v} = \mathbf{v}_l + \mathbf{v}_e \\ \mathbf{v}_e = \boldsymbol{\omega} \times \mathbf{r}_2 \end{cases} \tag{2.27}$$

where $\mathbf{v}_e$ is caused by the nozzle's eccentric rotation motion, and $\mathbf{v}_l$ is the radial velocity due to impingement. When the diameter of the nozzle equals 1 mm, the eccentric distance e is 0.5 mm and $|\boldsymbol{\omega}|$ is 1 rps, computed $|\mathbf{v}_e|$ is 6.3×10^{-3} m/s, which is too small compared with the velocity of the jet ($|\mathbf{v}_l|$ is about 20 m/s), thus it can be ignored. Therefore, the $\mathbf{v}$ can be briefly described as $\mathbf{v}_l$.

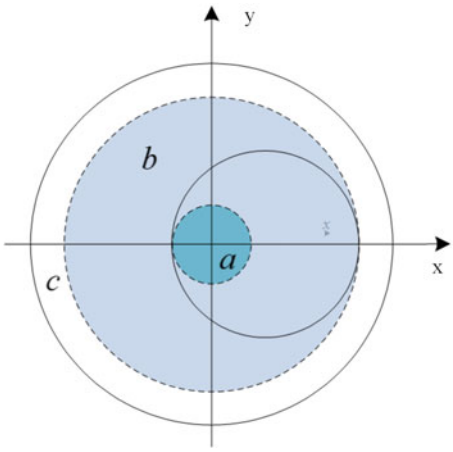

Fig. 2.29 Three areas in the polishing shape

Polishing shape can be expressed in three different areas, as shown in Fig. 2.29. The first area a is a circular shape with a radius $(r - e)$ around the point o_1, and footprint of the jet always covers on it in a period. The second area b is an annular shape, the radius of torus is from $(r - e)$ to $(r + e)$, and the effective range of polishing for an arbitrary point in this area is only the segment $(-\theta', \theta')$ in a period. The last area c is invalid. The material removal at the point $p(r_2,\theta_1)$ inside the polishing area in a period can be expressed as

$$R_1(r_2) = \int_{t_1}^{t_2} R(d,\theta)\mathrm{d}t = \frac{1}{\omega}\cdot\begin{cases}\int_{-\pi}^{\pi} R(d,\theta)\mathrm{d}\theta_1, & 0 \le r_2 \le r - e;\\ \int_{-\theta'}^{\theta'} R(d,\theta)\mathrm{d}\theta_1, & r - e < r_2 < r + e;\\ 0, & \text{others.}\end{cases} \tag{2.28}$$

Therefore, Eq. (2.28) can be described in a simple way:

$$R_1(r_2) = \frac{1}{\omega}\cdot\int_{-\overline{\theta}}^{\overline{\theta}} R(d,\theta)\mathrm{d}\theta_1 \tag{2.29}$$

where

$$\begin{cases}\overline{\theta} = \arccos\left\{\left[\left(r_2^2 + e^2 - r^2\right)/(2r_2e)\cdot \mathrm{rect}[(r_2 - r)/(2e)] - \mathrm{step}\left(r - e - r_2\right)\right\};\\ d = \left(e^2 + r_2^2 - 2er_2\cos\theta_1\right)^{1/2};\ \ 0 \le r_2 < r + e;\\ \theta = \arcsin(r_2\sin\theta_1/d).\end{cases}$$

2.3.3.2 Optimization of Parameters

Figure 2.30 shows the removal characters of magnetorheological jet polishing (MJP) with eccentric rotation motion. Figure 2.30a shows the normalized removal

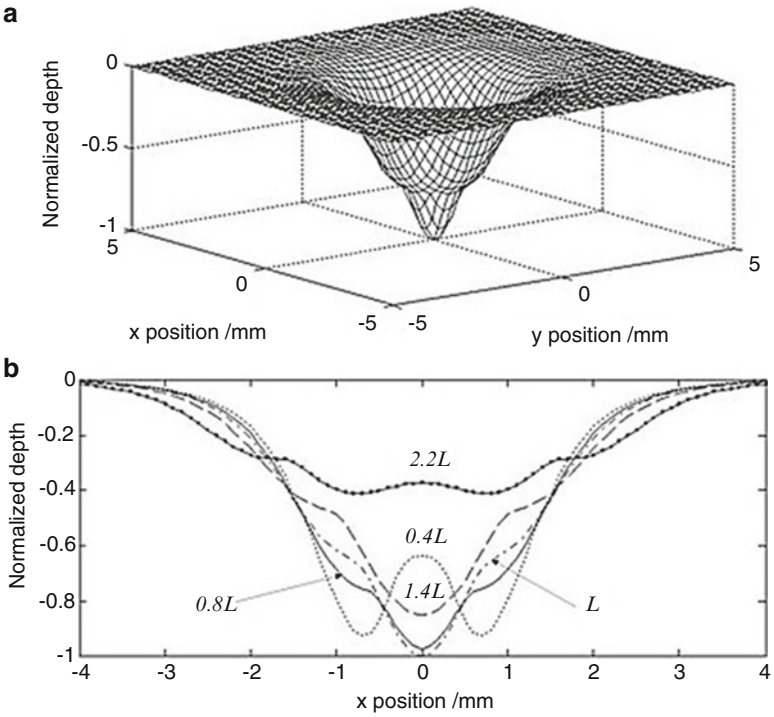

Fig. 2.30 Removal characters with eccentric rotation motion. (**a**) Removal shape with eccentric distance (L) and angular velocity (1 rps); (**b**) 2D profile sections across removal areas with different eccentric distances. *2D* two-dimensional

shape with eccentric distance L (as shown in Fig. 2.26) and angular velocity (1 rps), the removal shape has the maximum depth at the center and reduces to zero at the margin. Distribution of the removal shape possesses Gaussian-like character. The removal characters are then simulated with different eccentric distances (0.4L, 0.8L, L, 1.4L, and 2.2L); results are shown in Fig. 2.30b. Sectional curve with eccentric distance (0.4L) shows W-shape, but removal depth is not zero and it rises dramatically in the center. Removal distributions with eccentric distances (0.8L, L, and 1.4L) possess the character of Gaussian, but they have different depths and widths. Removal distribution is U-shaped when eccentric distance equals 2.2L. Overall, the depth first increases then decreases and the width gradually increases, with the eccentric distance being larger.

In order to find out the excellent eccentric distance, a tending gene F is put forward to estimate the optimal eccentric distance. A higher value of F means the character closely approximates to the ideal Gaussian distribution. As described by Wang et al. [13], the F is expressed as below.

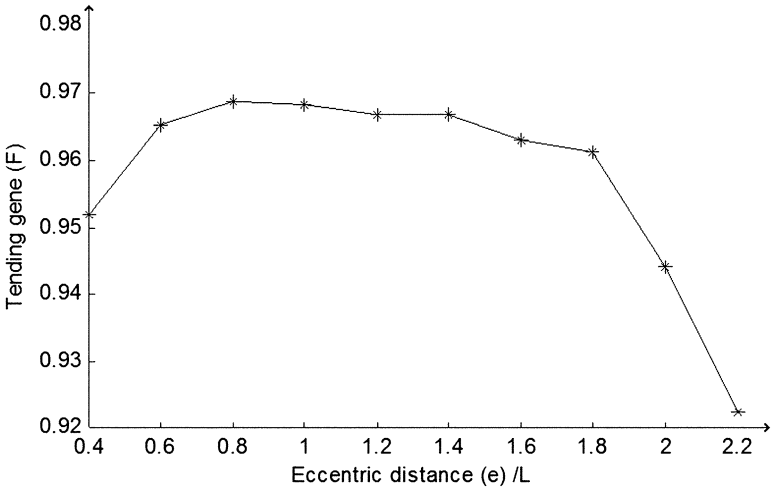

Fig. 2.31 The tending gene of material removal with different eccentric distance

$$F = \frac{W_{1/2}}{W} \tag{2.30}$$

where F is the tending gene, $W_{1/2}$ is the material removal in circular area with the half radius of the polishing spot around the center point, and W is the whole of the material removal.

For each different eccentric distance, the corresponding value of F is calculated and plotted in Fig. 2.31b. It is obvious that the distribution of the values is non-linear and unimodal distribution between $0.4L$ and $2.2L$, and the values of F are close to each other between $0.6L$ and $1.8L$. In particular, the maximum of F is 96.9 % (higher than 0.86 in the studies of Wang et al. [13]), when e is equal to $0.8L$. In addition, as seen in Fig. 2.30, the removal character possesses Gaussian-like character for $0.8L$. These indicate that $0.8L$ is the optimal eccentric distance and the removal character for $e = 0.8L$ is the optimal distribution.

2.3.3.3 Experimental Validation

Efforts have been made to find out the correlation between the experimental removal rate and the theoretical model with the self-made tool. K9 glasses with a diameter of 50 mm are used as the workpiece. The experimental settings are listed in Table 2.9.

With the above parameters, plenty of experimental studies with different distances have been conducted on the K9 glass with peak-to-valley (PV) 0.168 λ and root mean square (RMS) 0.031 λ ($\lambda = 632.8$ nm), as shown in Fig. 2.32.

Table 2.9 Parameters of polishing experiments

Parameter	Value
Mass fraction of CeO_2 particles in fluid (%)	6
Diameter of CeO_2 particle (μm)	2
Diameter of nozzle (mm)	1
Current (mA)	280
Number of turns in coil	4,000
Interior diameter of coil (mm)	6
Outside diameter of coil (mm)	18
High of coil (mm)	36
Diameter of wire (mm)	0.26
Pressure (MPa)	0.6

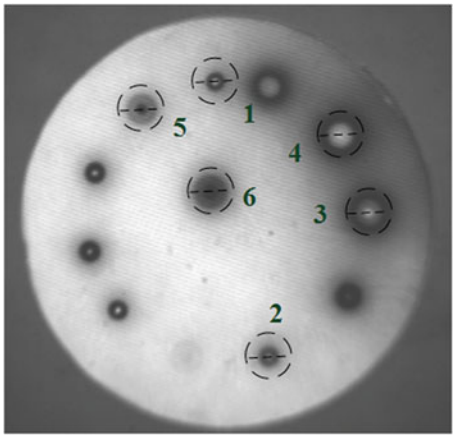

Fig. 2.32 Image showing the spots on the K9 glass

The six spots that are marked in Fig. 2.32 are the main objects of study. The first is the normal spot with the motionless tool. The remaining five spots show the shapes of polishing spots with eccentric rotation motion; their eccentric distances are about 0.4*L*, 0.8*L*, *L*, 1.4*L*, and 2.2*L*. The mask is necessary for researching the shape of the details, and the profiles across the removal areas are measured by ZYGO interferometer. Figure 2.33 shows the experimental results on the K9 glass for the profile curves of the polishing spots versus different eccentric distance.

Figure 2.33 shows the profile curves of the spots on K9 glass with a different jetting method (in each sub-graph, curve 1 and curve 2 indicate experimental and simulated data, respectively). Figure 2.33a shows the profile curve of the normal spot when the polishing tool maintains standstill. It has a peak in the middle and two valleys symmetrically at the adjacent margin. Besides, the curve accords with the distribution in Fig. 2.33, and its *L* equals approximately 0.7 mm. Figure 2.33b shows the degenerative W-shape in the second area when the eccentric distance is about 0.4*L*, the middle peak is reduced. The Gaussian-like curve would guarantee a successful polishing with the eccentric distance about 0.8*L*, which has maximum

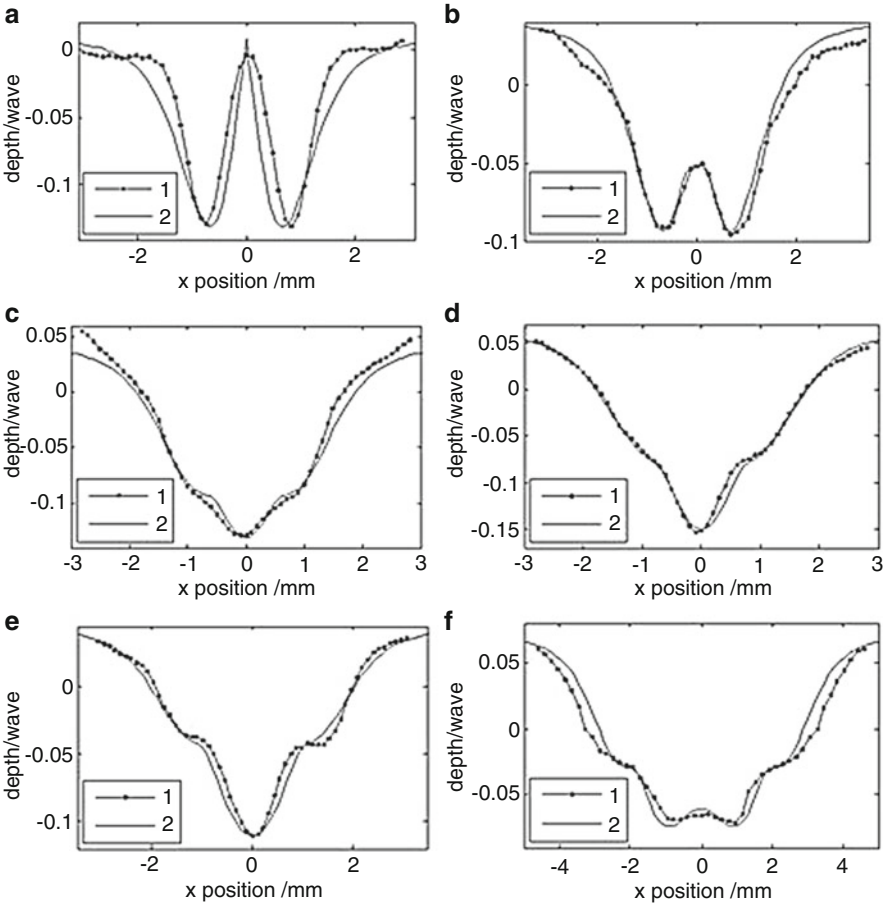

Fig. 2.33 The profile curves of the spots on K9 glass with different jetting method. (**a**) Normal spot; (**b**) eccentric distance is about 0.4*L*; (**c**) eccentric distance is about 0.8*L*; (**d**) eccentric distance is about *L*; (**e**) eccentric distance is about 1.4*L*; (**f**) eccentric distance is about 2.2*L*

removal at the center and reduces gradually, with the radius increasing. In particular, it is easy to observe that the curve varies smoothly, as shown in Fig. 2.33c. In Fig. 2.33d, the distribution of the profile is shown when the eccentric distance is about L, it is similar to the result of $0.8L$, but there are step-shaped distributions between the center and margin. Step-shaped distributions are more obvious in Fig. 2.33e when the eccentric distance is about $1.4L$. With the eccentric distance increasing, great changes have taken place in the distribution of the removal curve, as shown in Fig. 2.33f. It possesses not only the obvious step-shaped distributions but also a small protuberance in the middle.

According to above analysis, it is important to notice that in this case the profiles have been obtained in two different ways (experiment and simulation) resulting in the similar shapes.

2.3.4 Electrorheological Finishing

2.3.4.1 Model Constructions

Notwithstanding many years of investigation, there are still drawbacks in existing electrorheological (ER) polishing tools which restrict their practical applications. Traditional point-type tools contain only one of the electrodes in ER polishing. For a non-conductor workpiece, an auxiliary electrode needs to be placed close to the surface of the workpiece. This implies custom-made electrodes may be needed in some polishing work. Also, its location changes relative to the auxiliary electrode, when the tool is moved about onto the workpiece to polish. As the electric field changes with the tool location, this can result in a rather unstable removal and polishing performance.

ER fluids are usually non-conducting and have low viscosity. Viscosity increases significantly when an electric field is applied. ER fluids contain ER particles. These particles are perceived to form aggregates which align with the electric field, causing the ER fluid to change instantly from liquid to visco-plastic solid.

When an electric field is setup near the tip of a polishing tool and the tool is immersed in an ER fluid, the fluid within the influence of the field becomes viscous and effectively forms a small flexible polishing pad at the tool tip. With the addition of abrasive particles to the ER fluid, the abrasive particles are attracted to the ER particles in this virtual pad due to electrostatics. Under movement of the tool relative to the work surface, the abrasive particles are dragged through the gap between the tool and the surface, resulting in removal of asperities of the surface.

Within a certain range, field strength plays a dominant role in the viscosity of the ER fluid and in the attraction of abrasive particles to the ER particles. Thus, producing of a strong electric field at the tool tip is critical to the realization of ER polishing. An important application of ER polishing is in the polishing of small optics to high surface finishing. Quite often, such surfaces are non-conducting. They cannot be conveniently used as one of the electrodes in ER polishing [14]. An ER polishing tool with probe-like integrated-electrodes is proposed in this paper, aiming at the polishing of small non-conducting surfaces. The design concept is illustrated in the schematic diagram (Fig. 2.34). The central shaft (cathode) and the sleeve (anode) are exposed at the tool tip. ER fluid forms a virtual polishing pad near the tip when there is electrical potential difference between the two electrodes. Rotation of the central shaft causes the pad and the attached abrasive particles to also rotate and affects polishing action. There is no need for any additional electrodes for electric field formation.

A setup for ER polishing was built based on this design. The setup consists of a high-voltage power supply, a two-axis controller and a tool head (Fig. 2.35a). Key components of the tool head are the drive, translation device, and polishing device (Fig. 2.35b).

The device was firmly constructed. The three connecting rods and the upper and lower discs form the base frame of the polishing device. A motor on the upper disc is connected to the central shaft through a coupler.

A schematic of the lower part of the polishing device is given in Fig. 2.36a. A cone-shaped conducting sleeve is installed in the center of the lower disc, and the

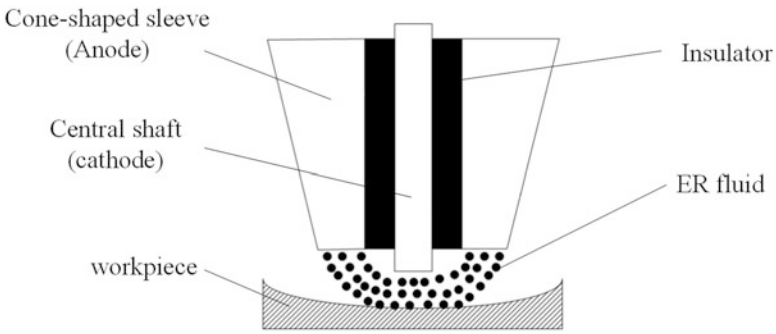

Fig. 2.34 Schematic diagram of design concept

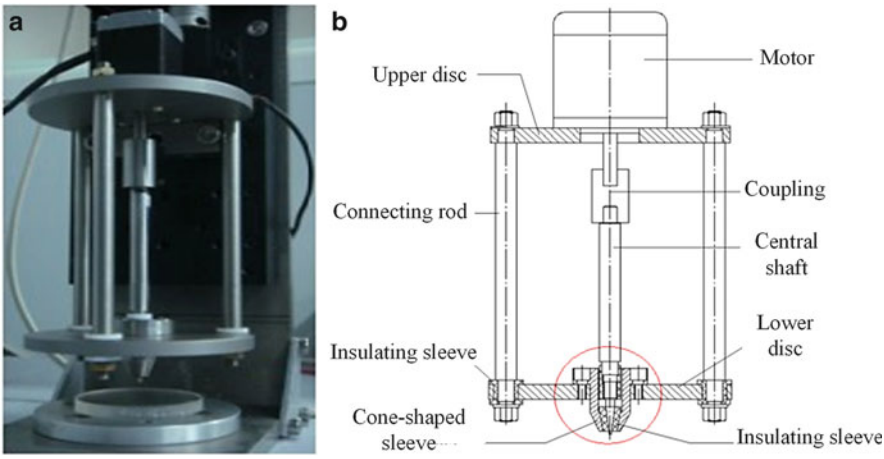

Fig. 2.35 ER polishing equipment. (**a**) Polishing device; (**b**) tool head

central shaft passes through the center of the cone-shaped sleeve. The central shaft serves as the cathode and is connected to the ground. The cone-shaped sleeve is the anode. An insulating sleeve is mounted on to the tip of the central shaft to prevent short circuiting when powered on. Rotary parts are accurately fabricated, well aligned, and supported to reduce vibration during processing.

In Fig. 2.36a, l is the distance of the central shaft beyond the cone-shaped sleeve, a is the diameter of the central shaft at the tip, and b and c are the inner and outer diameters of the cone-shaped sleeve. In the current setup, $l = 1$ mm, $a = 1.4$ mm, $b = 5.4$ mm, and $c = 8$ mm, respectively.

A photo of the tool head in action is shown in Fig. 2.36b. The tool head was positioned close to a specimen, and ER fluid was applied to the vicinity. Once the potential difference was established between the two electrodes, ER fluid became viscous and was seen attracted to the exposed part of the central shaft. An elevated ring of ER fluid was formed after the central shaft was set to rotate, which may be

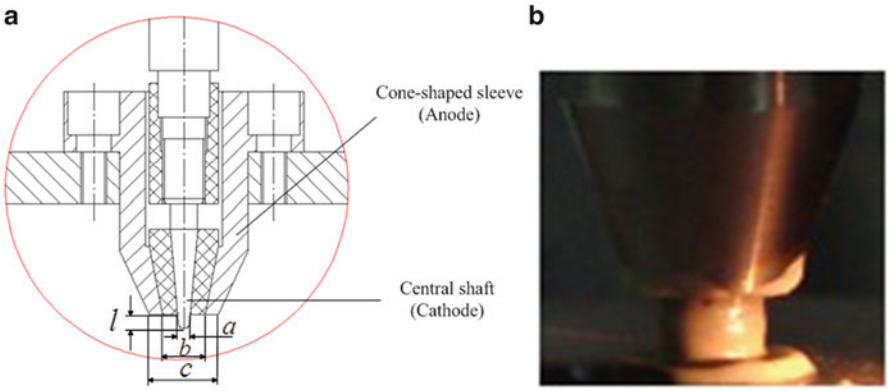

Fig. 2.36 Magnified views of the lower part of the polishing device. (**a**) schematic diagram; (**b**) polishing in process

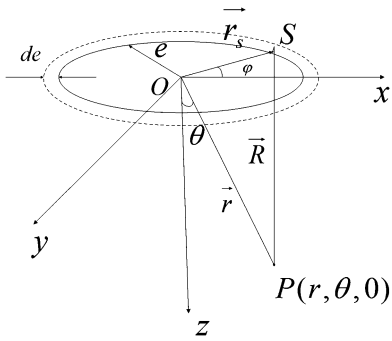

Fig. 2.37 Coordinate system of the anode ring

seen as a balance of gravitational force, centrifugal force, surface tension, and field-induced dipole attraction. The diameter of that ring was approximately 4 mm, slightly smaller than the inner diameter of the sleeve anode.

ER polishing effect is directly related to the strength of the electric field. In this section, the field strength near the tool tip is analyzed. The anode and the cathode are electrically charged when they are respectively connected to the two terminals of a voltage supply. The electric field strength in the vicinity of the tool tip depends on the shape and size of the anode and the cathode, and on the charge distribution. The field strength is analyzed based on Coulomb's law and making use of the superposition principle of electric fields. The effects of the anode and the cathode are considered separately and are then combined.

The bottom-end face of the anode is flat and annular (Fig. 2.37). Electric charge is assumed to be evenly distributed on the end face.

For the coordinate frame shown in the figure, the origin O is at the center of the end face and the Z-axis is along the centerline of central shaft. Consider a point $P(r,\ \theta,\ \Phi = 0)$ on the $x-z$ plane, with r, θ, and Φ being the radial distance,

inclination angle, and azimuth angle, respectively. The position of P may be expressed as $\vec{r} = r\sin\theta\,\vec{i} + r\cos\theta\,\vec{k}$.

The end face of the anode may be seen as consisted of concentric rings. Consider the ring of radius e with infinitesimal width de. Let S be a small region of the ring at azimuth φ and the angle subtended at the origin is $\mathrm{d}\varphi$. The position of S is $\vec{r}_s = e\cos\varphi\,\vec{i} - e\sin\varphi\,\vec{j}$. The position of P relative to S is then given by:

$$\vec{R} = \vec{r} - \vec{r}_s = (r\sin\theta - e\cos\varphi)\cdot\vec{i} + e\sin\varphi\cdot\vec{j} + r\cos\theta\cdot\vec{k} \tag{2.31}$$

$$\left|\vec{R}\right| = \sqrt{e^2 + r^2 - 2er\sin\theta\cos\varphi} \tag{2.32}$$

If the charge density on the end surface of the anode is σ, the charge on S can then be expressed as $\mathrm{d}q = \sigma\cdot e\mathrm{d}\varphi\cdot\mathrm{d}e$. According to Coulomb's law, the electrical field strength at point P due to the charge on S is:

$$\begin{aligned}\mathrm{d}\vec{E} &= \frac{\vec{R}\,\mathrm{d}q}{4\pi\varepsilon\left|\vec{R}\right|^3} \\ &= \frac{\left[(r\sin\theta - e\cos\varphi)\cdot\vec{i} + e\sin\varphi\cdot\vec{j} + r\cos\theta\cdot\vec{k}\right]\sigma\cdot e\cdot\mathrm{d}e\cdot\mathrm{d}\varphi}{4\pi\varepsilon(e^2 + r^2 - 2er\sin\theta\cos\varphi)^{3/2}}\end{aligned} \tag{2.33}$$

where ε is the permittivity of the medium.

The electrical field at P due to the anode is:

$$\vec{E}_+ = \int_{b/2}^{c/2}\int_0^{2\pi}\mathrm{d}E = E_{x+}\vec{i} + E_{y+}\vec{j} + E_{z+}\vec{k} \tag{2.34}$$

where the three components of the field are, respectively:

$$E_{x+} = \frac{\sigma}{4\pi\varepsilon}\int_{b/2}^{c/2}\int_0^{2\pi}\frac{(x - e\cos\varphi)\cdot e\cdot\mathrm{d}e\cdot\mathrm{d}\varphi}{(e^2 + x^2 + z^2 - 2ex\cos\varphi)^{3/2}} \tag{2.35}$$

$$E_{y+} = \frac{\sigma}{4\pi\varepsilon}\int_{b/2}^{c/2}\int_0^{2\pi}\frac{e\sin\varphi\cdot e\cdot\mathrm{d}e\cdot\mathrm{d}\varphi}{(e^2 + x^2 + z^2 - 2ex\cos\varphi)^{3/2}} = 0 \tag{2.36}$$

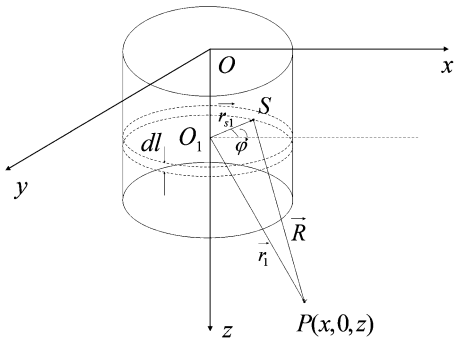

Fig. 2.38 Coordinate system of the cathode ring

$$E_{z+} = \frac{\sigma}{4\pi\varepsilon} \int_{b/2}^{c/2} \int_{0}^{2\pi} \frac{z \cdot e \cdot \mathrm{d}e \cdot \mathrm{d}\varphi}{\left(e^2 + x^2 + z^2 - 2ex\cos\varphi\right)^{3/2}} \tag{2.37}$$

The side of the central shaft which extends beyond the cone-shaped sleeve is approximately cylindrical (Fig. 2.38). Electric charge of the cathode is assumed to be evenly distributed on the surface of this extended part of the central shaft.

For the coordinate frame shown in the figure, the origin O is at the same level as the end face of the sleeve, and the Z-axis is along the centerline of the central shaft. Consider a point $P(x,0,z)$ on the x–z plane and a ring centered at O_1 with infinitesimal height dl. The position of P relative to the ring center is given by $\vec{r_1} = (x, 0, z-l)$. Let S be a small region of the ring at azimuth φ and the angle subtended at the O_1 is dφ. The position of S relative to O_1 is $\vec{r_{s1}} = \frac{a}{2} \cdot \cos\varphi \vec{i} - \frac{a}{2} \cdot \sin\varphi \vec{j}$. The position of P relative to S is then given by:

$$\vec{R} = \vec{r_1} - \vec{r_{s1}} = \left(x - \frac{a}{2}\cos\varphi\right)\vec{i} + \frac{a}{2}\sin\varphi\vec{j} + (z-l)\vec{k} \tag{2.38}$$

$$\left|\vec{R}\right| = \sqrt{x^2 + \left(\frac{a}{2}\right)^2 - ax\cos\varphi + (z-l)^2} \tag{2.39}$$

If the charge density on the cathode is η, the charge on S can then be expressed as $\mathrm{d}q = -\eta \cdot \frac{a}{2}\mathrm{d}\varphi \cdot \mathrm{d}l$. According to Coulomb's law, the electric field strength at point P due to the charge on S is:

$$\mathrm{d}\vec{E} = \frac{\vec{R}\,\mathrm{d}q}{4\pi\varepsilon\left|\vec{R}\right|^3} = \frac{-\left[\left(x - \frac{a}{2}\cos\varphi\right)\vec{i} + \frac{a}{2}\sin\varphi\vec{j} + (z-l)\vec{k}\right]\eta \cdot \frac{a}{2} \cdot \mathrm{d}\varphi \cdot \mathrm{d}l}{4\pi\varepsilon\left[x^2 + \left(\frac{a}{2}\right)^2 - ax\cos\varphi + (z-l)^2\right]^{3/2}} \tag{2.40}$$

The electrical field at P due to the cathode is:

$$\vec{E}_{-} = \int_0^l \int_0^{2\pi} \mathrm{d}\vec{E} = E_{x-}\vec{i} + E_{y-}\vec{j} + E_{z-}\vec{k} \tag{2.41}$$

where the three components of the field are, respectively:

$$E_{x-} = -\frac{a\eta}{8\pi\varepsilon} \int_0^l \int_0^{2\pi} \frac{\left(x - \frac{a}{2}\cos\varphi\right) \cdot \mathrm{d}\varphi \cdot \mathrm{d}l}{\left[x^2 + \left(\frac{a}{2}\right)^2 - ax\cos\varphi + (z-l)^2\right]^{3/2}} \tag{2.42}$$

$$E_{y-} = -\frac{a\eta}{8\pi\varepsilon} \int_0^l \int_0^{2\pi} \frac{\frac{a}{2}\sin\varphi \cdot \mathrm{d}\varphi \cdot \mathrm{d}l}{\left[x^2 + \left(\frac{a}{2}\right)^2 - ax\cos\varphi + (z-l)^2\right]^{3/2}} \tag{2.43}$$

$$E_{z-} = -\frac{a\eta}{8\pi\varepsilon} \int_0^l \int_0^{2\pi} \frac{(z-l) \cdot \mathrm{d}\varphi \cdot \mathrm{d}l}{\left[x^2 + \left(\frac{a}{2}\right)^2 - ax\cos\varphi + (z-l)^2\right]^{3/2}} \tag{2.44}$$

Because of the conservation of electric charge, the charge on the anode is equal to the charge on the cathode. Thus, one has:

$$\sigma \cdot s_{+} = \eta \cdot s_{-} \tag{2.45}$$

where $s_{+} = \pi[(c/2)^2 - (b/2)^2]$ and $s_{-} = a \cdot l \cdot \pi$ are, respectively, the effective surface area of the anode and the cathode.

For the case of two parallel plates, the electric field is considered uniform and one has:

$$\frac{U}{d} = \frac{\sigma}{\varepsilon} \Rightarrow \sigma = \frac{U\varepsilon}{d} \tag{2.46}$$

where d is the distance between the plates and U is the potential difference. This is assumed to be applicable for the calculation of σ with $d = (b - a)/2$, which is the gap between the central shaft and the cone-shaped sleeve. The assumption of parallel plates is reasonably accurate below the sleeve and near the lower end of the central shaft where polishing takes place.

By the principle of superposition, the combined field:

$$\begin{aligned} \vec{E} &= E_x\vec{i} + E_y\vec{j} + E_z\vec{k} \\ &= (E_{x+} + E_{x-})\vec{i} + \left(E_{y+} + E_{y-}\right)\vec{j} + (E_{z+} + E_{z-})\vec{k} \end{aligned} \tag{2.47}$$

$$E_x = \frac{U}{8\pi}\int_{2.7}^{4}\int_{0}^{2\pi}\frac{(x - e\cos\varphi)\cdot e\cdot \mathrm{d}\varphi\cdot \mathrm{d}e}{(e^2 + x^2 + z^2 - 2ex\cos\varphi)^{3/2}} - \frac{0.544U}{\pi}$$

$$\int_{0}^{1}\int_{0}^{2\pi}\frac{(x - 0.7\cos\varphi)\cdot \mathrm{d}\varphi\cdot \mathrm{d}l}{\left[x^2 + 0.49 - 1.4x\cos\varphi + (z-l)^2\right]^{3/2}} \tag{2.48}$$

$$E_y = 0 \tag{2.49}$$

$$E_z = \frac{U}{8\pi}\int_{2.7}^{4}\int_{0}^{2\pi}\frac{z\cdot e\cdot \mathrm{d}e\cdot \mathrm{d}\varphi}{(e^2 + x^2 + z^2 - 2ex\cos\varphi)^{3/2}}$$

$$-\frac{0.544U}{\pi}\int_{0}^{1}\int_{0}^{2\pi}\frac{(z-l)\cdot \mathrm{d}\varphi\cdot \mathrm{d}l}{\left[x^2 + 0.49 - 1.4x\cos\varphi + (z-l)^2\right]^{3/2}} \tag{2.50}$$

The field strength:

$$E = \left|\vec{E}\right| = \sqrt{E_x^2 + E_z^2} \tag{2.51}$$

When the point P is along the Z-axis, the electric field strength can be analytically solved as:

$$E = \frac{U\cdot z}{4}\left(\frac{1}{\sqrt{7.29 + z^2}} - \frac{1}{\sqrt{16 + z^2}}\right) - 1.089\cdot U\left(\frac{1}{\sqrt{0.49 + (z-1)^2}} - \frac{1}{\sqrt{0.49 + z^2}}\right) \tag{2.52}$$

Based on the above equation, changes of the field strength along the Z-axis with respect to the distance from the tip of the central shaft are shown in Fig. 2.39. The supply voltage varies from 3,000 to 1,500 V. The tip of the shaft is at $z = 1$ mm. The field strength is proportional to the supply voltage. It is strongest at the tip and decreases away from the tip. At a distance of 1 mm from the tip, the field strength is approximately half of it maximum value at the tip.

The electric field near the tool tip is also simulated using finite element analysis. Parameters used in the simulations are tabulated in Table 2.10. Simulation results are shown in Fig. 2.40. At the maximum supply voltage of 3,000 V, the maximum field strength is 2.46×10^6 V/m. The field strength decreases monotonically with the supply voltage. Field strength is particularly high near the edge of the central shaft and the inner edge of the end face of the sleeve, which can be explained by charge concentration at the edges. Yet, one can see that such effects diminish rather

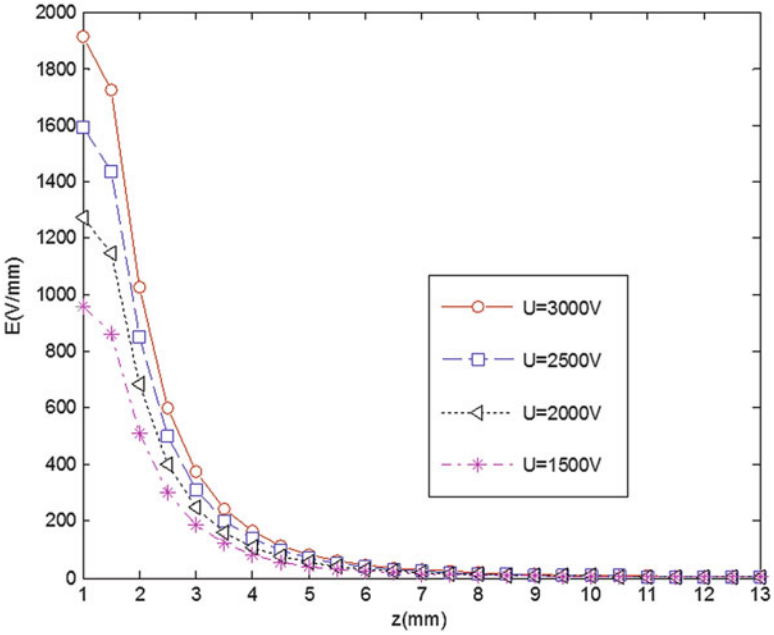

Fig. 2.39 Simulation of the electric field strength along the *Z*-axis

Table 2.10 Finite element analysis parameters

Material	Steel 0Cr18Ni9	Material resistivity	$9.7 \times 10^{-8}\Omega \cdot m$
Air resistivity	$10^{6}\Omega \cdot m$	Cathode voltage	0 V
Anode voltage	1,500, 2,000, 2,500, 3,000 V		
Element type	Field analysis unit 67 with center of symmetry and far-field analysis unit 110		

rapidly from the edges and they are not noticeable beyond a small fraction of a millimeter from the edges. Overall, the field strength decreases quickly away from the tip of the central shaft, which is consistent with the analytical model of the electric field developed above and the results in Fig. 2.39. These also suggest the assumptions of uniform distribution of charge on the surface of the anode and the cathode are acceptable, and the analytical model provides reasonable prediction of the field strength as long as the point of interest is not within a small fraction of the edges.

2.3.4.2 Polishing Experiments

Experiments were conducted to examine the usefulness of the proposed tool with integrated electrodes for the polishing of non-conducting optics. The rate of

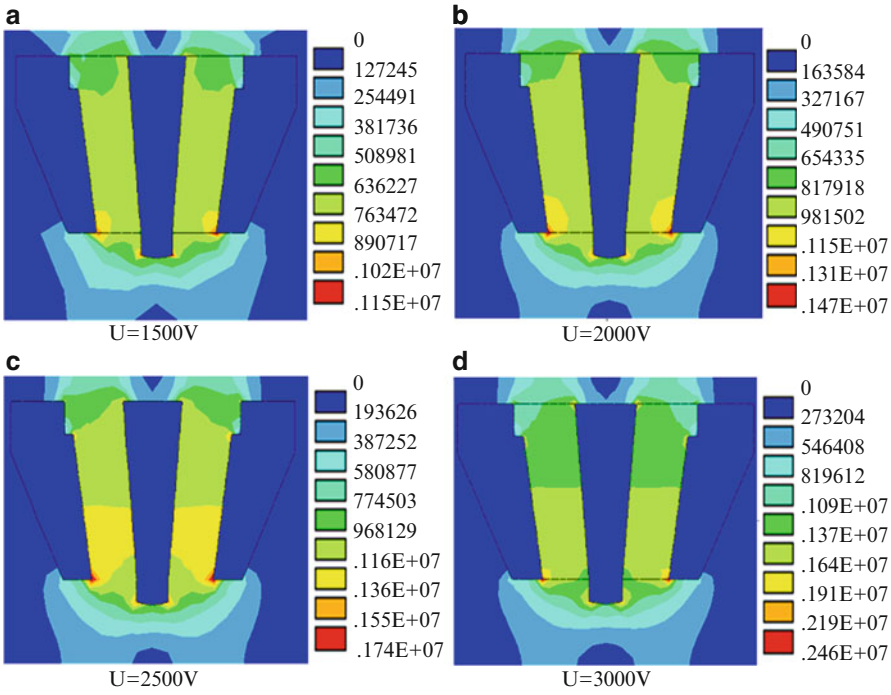

Fig. 2.40 Finite element analysis of electric field around the tool head

material removal is expected to increase with the field strength [11]. Two parameters to be studied in the current experiments are the supply voltage and the operating distance. In the last section, they were shown to have strong influence on the field strength. Their effects on ER polishing were investigated.

The ER fluid used in the experiments was composed of 47.62 % starch, 47.62 % silicone oil, and 4.76 % ceria. For all experiments, the rotating speed of the central shaft was set at 1,500 rpm and the polishing time was set at 30 min. The tool was perpendicular to the specimen. The specimens were made of K9 glass and were prepared using traditional grinding and polishing to a level of finishing suitable for the experiments.

The supply voltage was 2,000 V, and the operating distance varied between 0.5 and 0.8 mm. The surface morphology of the specimens was measured before and after ER polishing with a FISBA-μ820 interferometer. The measured area was set at 10.7 mm × 9.6 mm, which was slightly smaller than the impression on the specimen by the tool. The CCD resolution of 1,024 × 1,020 pixels was suitable for form or waviness measurement or surface irregularities investigation over a larger range.

The captured surface profiles are shown in Fig. 2.41. Polishing leads to material removal. There is clear evidence that such removal in ER polishing can smooth the surface profiles and reduce the PV values.

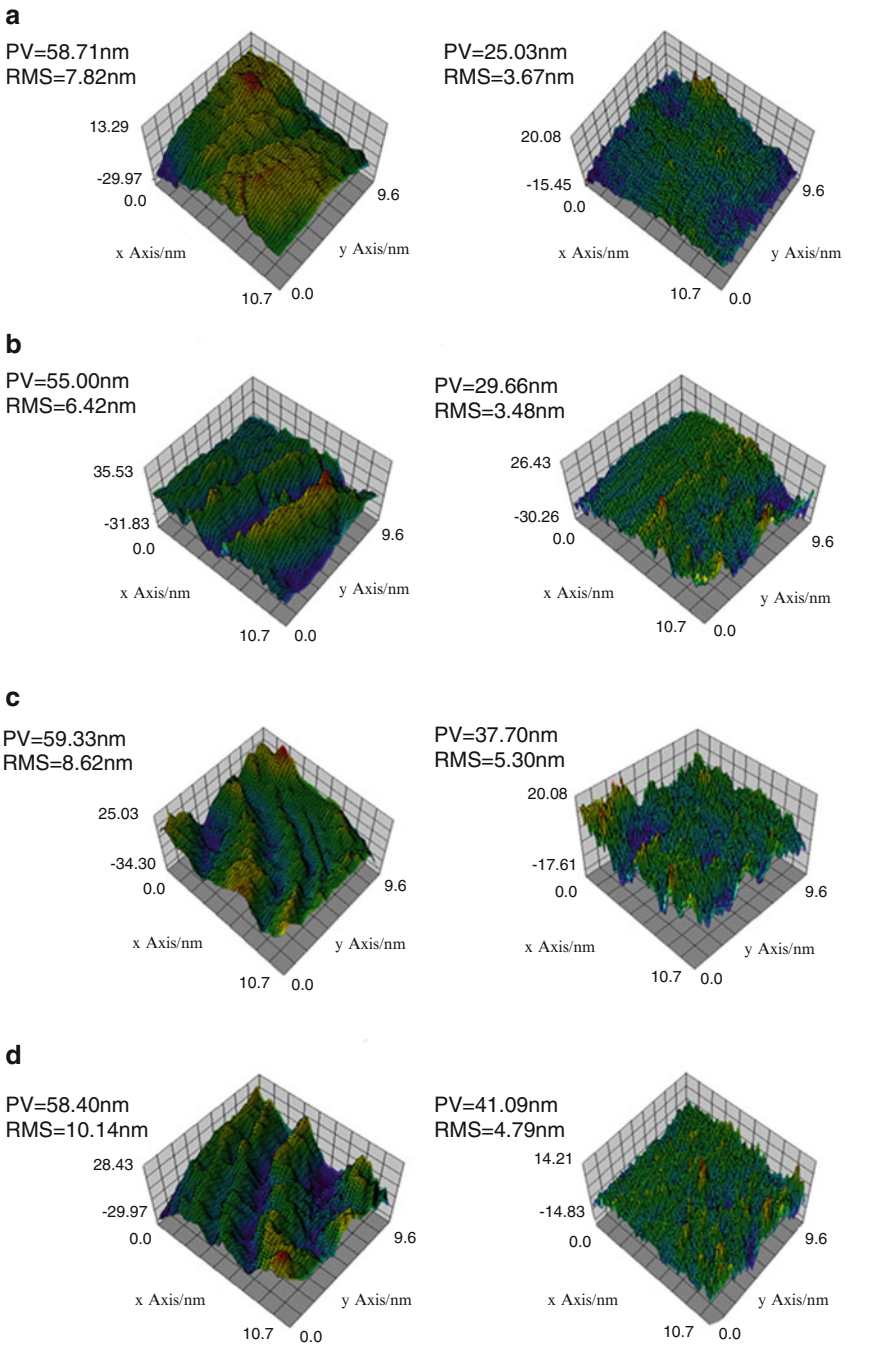

Fig. 2.41 Changes of the surface profile ($U = 2{,}000$ V). (**a**) $z = 0.5$ mm; (**b**) $z = 0.6$ mm; (**c**) $z = 0.7$ mm; (**d**) $z = 0.8$ mm

Table 2.11 Peak-to-valley versus z

z (mm)	Before (a_1) (nm)	After (a_2) (nm)	$a_1 - a_2$ (nm)	K (%)
0.5	58.71	25.03	33.68	57.37
0.6	55.00	29.66	25.34	46.07
0.7	59.33	37.70	21.63	36.46
0.8	58.40	41.09	17.31	29.64

One can observe more obvious polishing effect when the operating distance is shorter. The final PV is smaller and the reduction in PV is larger when the operating distance is shorter (Table 2.11). It is perceived that the ER fluid forms a virtual polishing pad around the tool tip, under the influence of the electric field. The stronger effects on the PV reduction when the operating distance is shorter suggest that the stiffness of the virtual pad increases closer to the tip of the tool. The increase in stiffness is attributed to the higher viscosity of the ER fluid closer to the tool tip because of the increase in field strength near the tip. The greatest reduction in PV obtained for the operating distance was 0.5 mm where the PV was reduced from 58.71 to 25.03 nm.

The relative change of an indicator is expressed as:

$$K = \frac{a_1 - a_2}{a_1} \tag{2.53}$$

where a_1 and a_2 are the values of the indicator before and after processing, respectively.

The relative change of PV is plotted against the operating distance in Fig. 2.42. The monotonic trend of the plot suggests the removal of surface irregularities is more effective and faster when the tool is closer to the specimen.

RMS of a surface profile gives more averaged measurement (Table 2.12). The relative change of RMS is also plotted against the operating distance in Fig. 2.42. The result also suggests a monotonic trend, except the case at the operating distance is 0.8 mm. Inspection of the surface profiles in Fig. 2.41 reveals that more material was indeed removed for the cases of the operating distance from 0.5 to 0.7 mm. The specimen for the 0.8 mm operating distance contained relatively more narrow ridges and grooves on the surface. It was likely that, for that specimen, a larger reduction in RMS could be achieved with less removal of material.

The operating distance was set at 0.5 mm, and the supply voltage varied between 1,500 and 3,000 V. The surface roughness Ra of the specimens was measured before and after ER polishing with a wyko NT1100 interferometer. The measured area covered 227 μm × 298.5 μm. The CCD resolution of 736 × 480 pixels was adequate for roughness measurement or surface irregularities investigation over a smaller range.

Comparison of the surface profile before and after polishing was shown in Fig. 2.43. Results indicate successful reduction of the surface roughness Ra in the nanometer range. In this range, resulting surface profiles did not resemble the original profiles. The Ra of the original surfaces was between 4.1 and 8.5 nm

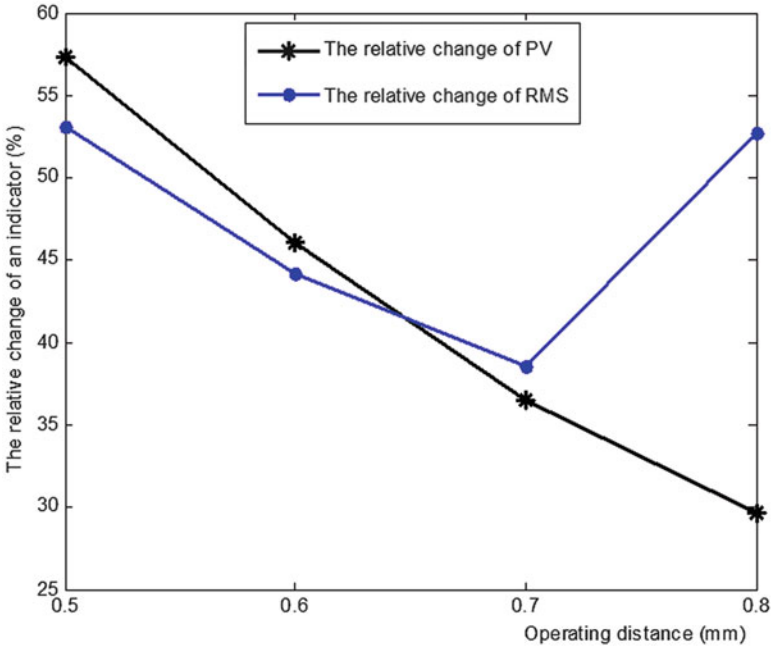

Fig. 2.42 Relationship between the relative change of PV and RMS and the operating distance ($U = 2{,}000$ V). *PV* peak-to-valley, *RMS* root square mean

Table 2.12 Root mean square versus z

z (mm)	Before (a_1) (nm)	After (a_2) (nm)	$a_1 - a_2$ (nm)	K (%)
0.5	7.82	3.67	4.15	53.07
0.6	6.24	3.48	2.76	44.23
0.7	8.62	5.30	3.32	38.52
0.8	10.14	4.79	5.35	52.76

(Table 2.13). The Ra of the resulting surfaces was between 2.5 and 2.8 nm, with the exception of the case of $U = 2{,}000$ V where Ra was 3.9 nm. These suggest that, within the voltage range, the supply voltage did not play a significant role in the achieved Ra. For the case of $U = 2{,}000$ V, one can see a long and broad ridge across the surface, which may be the reason for the higher Ra of 3.9 nm. A likely explanation is inhomogeneity of the specimen as all the other specimens seem to have rather unremarkable surface profiles after polishing.

The relative change of Ra is plotted against the supply voltage in Fig. 2.44. The effect on the rate of Ra reduction seems to be larger with a larger supply voltage. Relatively speaking, the effect is more distinct when the voltage is increased from 1,500 to 2,000 V, compared with the increase from 2,000 to 2,500 V. It is about to level off when the voltage is beyond 3,000 V.

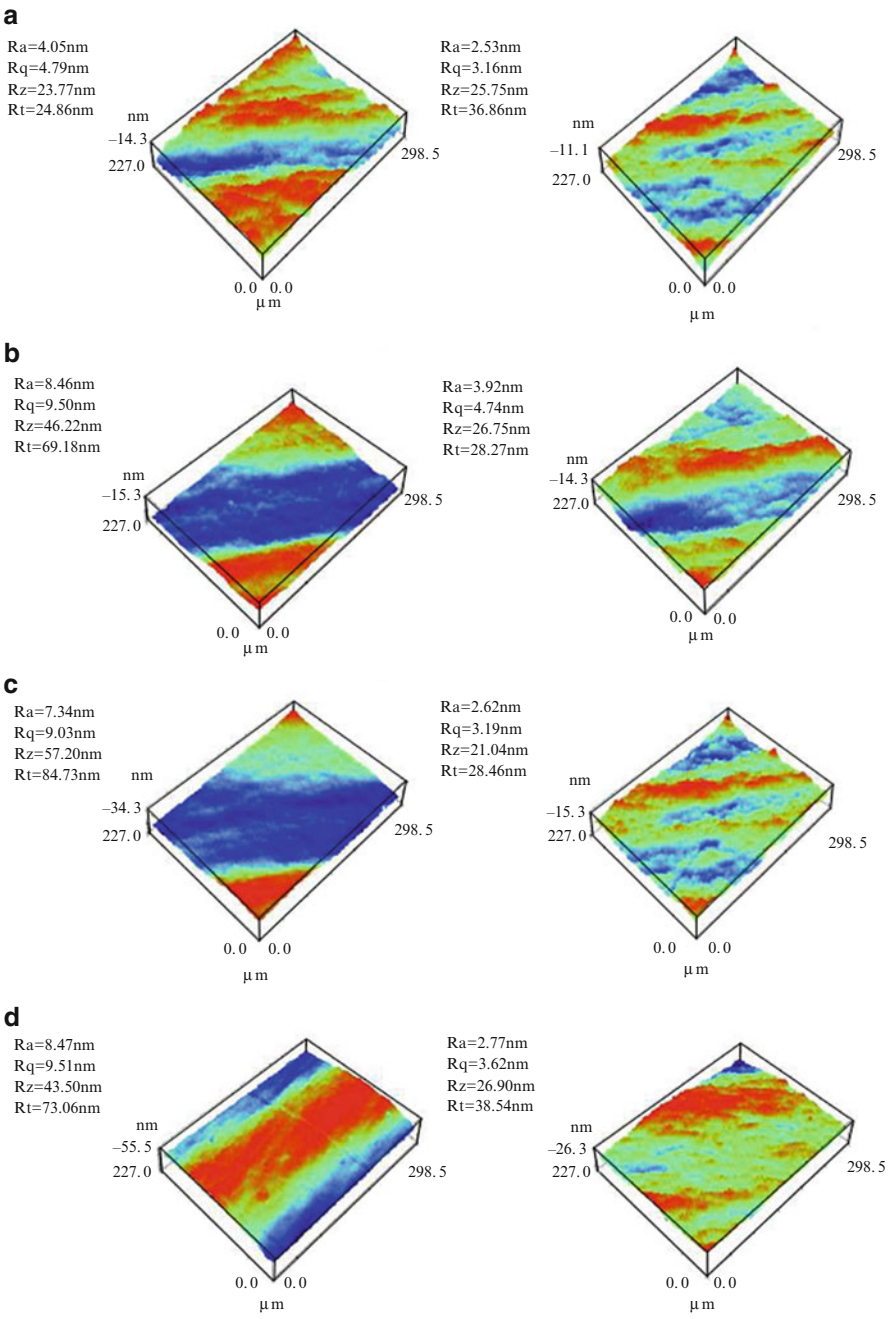

Fig. 2.43 Changes of the surface roughness (operating distance 1.5 mm)

Table 2.13 Roughness average (Ra) versus U

U (V)	Before (a_1) (nm)	After (a_2) (nm)	$a_1 - a_2$ (nm)	K (%)
1,500	4.05	2.53	1.52	37.53
2,000	8.46	3.92	4.54	53.66
2,500	7.34	2.62	4.72	64.31
3,000	8.47	2.77	5.70	67.30

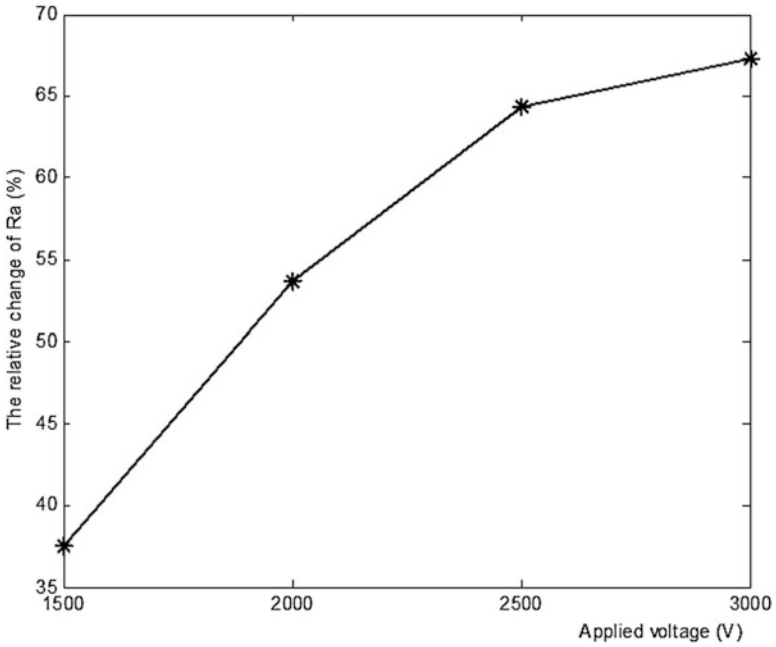

Fig. 2.44 Relationship between the relative change of roughness average (Ra) and the supply voltage (operating distance 0.5 mm)

Presence of abrasive particles in the ER fluid is important to material removal and Ra reduction. The rate of removal depends on the amount of abrasive particles in contact with the surface. A larger supply voltage seems to induce better attraction of the abrasive particles to the ER particle aggregates. Thus, higher rates of removal are obtained when the aggregates are rubbed against the surface, as they are carried by the rotation of the central shaft.

Leveling off of the curve in Fig. 2.44 indicates that further increase in the supply voltage cannot lead to further significant increase in removal rate. It is possible that further voltage increase did not help to attract additional abrasive particles. It is also possible that there was no further formation of ER particle aggregates.

In traditional polishing, the final Ra of a surface depends mainly on the size of the abrasive particles. To a lesser extent, it also depends on the force on the

polishing tool. In the current experiments, the final Ra did not vary notably with the supply voltage. This is reasonable as the same type of abrasives was used in all the experiments. Although the supply voltage affected the viscosity of the virtual pad and thus, to some extent, the indentation of abrasive particles, the effects on the Ra were negligible.

References

1. Juranek HJ, Sand R, Schweizer J, Harnisch B, Kunkel BP, Schmidt E, Litzelmann A, Schillke F, Dempewolf G (1998) Off-axis telescopes: the future generation of Earth observation telescopes. In: SPIE international symposium on optical science, engineering, and instrumentation. International Society for Optics and Photonics, Bellingham, pp 104–115
2. Rupp V (1965) The development of optical surfaces during the grinding process. Appl Opt 4(6):743–748
3. Jones RA (1977) Optimization of computer controlled polishing. Appl Opt 16(1):218–224
4. Cheng H, Feng Z, Wu Y (2004) Process technology of aspherical mirrors manufacturing with magnetorheological finishing. Mater Sci Forum 471–472:6–10
5. Cheng H, Yeung Y, Wang Y (2009) Experimentation on MR fluid using a 2-axis wheel tool. J Mater Pro Tech 209(12-13):5254–5261
6. Golini D (1999) Precision optics manufacturing using magnetorheological finishing (MRF). In: Singapore. International Society for Optics and Photonics, Bellingham, pp 78–85
7. Cheng H, Feng Z, Wang Y, Lei S (2005) Magnetorheological finishing of SiC aspheric mirrors. Mater Manuf Process 20(6):917–931
8. Chi C, Wang Z, Zhao P (1993) Iron magneto-fluid-mechanics. BeiHang University Press, Beijing, pp 378
9. Cheng HB, Wang T, Feng YP, Yam Y (2011) Process planning and tool design of magnetorheological jet finishing. Appl Mech Mater 44:222–226
10. Tricard M, Kordonski W, Shorey A, Evans C (2006) Magnetorheological jet finishing of conformal, freeform and steep concave optics. CIRP Ann Manuf Technol 55(1):309–312
11. Kordonski WI, Shorey AB, Tricard M (2006) Magnetorheological jet (MR Jet™) finishing technology. J Fluids Eng 128(1):20–26
12. Becker H, Hottel H, Williams G (1967) The nozzle-fluid concentration field of the round, turbulent, free jet. J Fluid Mech 30(2):285–303
13. Wang T, Cheng H, Dong Z, Tam H (2013) Removal character of vertical jet polishing with eccentric rotation motion using magnetorheological fluid. J Mater Pro Tech 213(9):1532–1537
14. Cheng H-B, Feng Z-J, Cheng K, Wang Y-W (2005) Design of a six-axis high precision machine tool and its application in machining aspherical optical mirrors. Int J Mach Tool Manuf 45(9):1085–1094

http://www.springer.com/978-3-642-45354-0

Independent Variables for Optical Surfacing Systems
Synthesis, Characterization and Application
Cheng, H.
2014, VI, 168 p. 150 illus., 105 illus. in color., Hardcover
ISBN: 978-3-642-45354-0